Mitochondrially Transcribed dsRNA Mediates Manganese-induced Neuroinflammation

Avanti Gokhale[1†], Hadassah Mendez-Vazquez[1†], Maureen M. Sampson[2], Felix G Rivera Moctezuma[7], Adriana Harbuzariu[3], Anson Sing[2], Stephanie A. Zlatic[1], Anne M. Roberts[4,5], Milankumar Prajapati[6], Blaine R. Roberts[4,5], Thomas B. Bartnikas[6], Levi B. Wood[7,8], Steven A. Sloan[2], Victor Faundez[1], Erica Werner[1#]

[†]**These authors contributed equally to this work.**

Abstract

Manganese (Mn) is an essential trace element required for various biological functions, but excessive Mn levels are neurotoxic and lead to significant health concerns. The mechanisms underlying Mn-induced neurotoxicity remain poorly understood. Neuropathological studies of affected brain regions reveal astrogliosis, and neuronal loss, along with evidence of neuroinflammation. Here, we present a novel Mn-dependent mechanism linking mitochondrial dysfunction to neuroinflammation. We found that Mn disrupts mitochondrial transcriptome processing, resulting in the accumulation of complementary RNAs that form double-stranded RNA (dsRNA). This dsRNA is released to the cytoplasm, where it activates cytosolic sensor pathways, triggering type I interferon responses and inflammatory cytokine production. This mechanism is evident in 100-day human cerebral organoids, where Mn-induced inflammatory responses are observed predominantly in mature astrocytes. Similar effects were observed in the transcriptome and cytokine profile of female and male mouse brains carrying mutations in the *SLC30A10* gene, a model of hypermanganesemia with dystonia1 disorder. These findings highlight a previously unrecognized role for mitochondrial dsRNA in Mn-induced neuroinflammation and provide insights into the molecular pathogenesis of manganism. We propose that this mitochondrial dsRNA-induced

inflammatory pathway could be active in other diseases caused by environmental or genetic factors.

Author affiliations:

1 Department of Cell Biology, Emory University, Atlanta, GA, USA, 30322

2 Department of Human Genetics, Emory University, Atlanta, GA, USA, 30322

3 Emory Stem Cell and Organoids Core, Emory University, Atlanta, GA, USA, 30322

4 Department of Biochemistry, Emory University, Atlanta, GA, USA, 30322

5 Department of Neurology, Emory University, Atlanta, GA, USA, 30322

6 Department of Pathology and Laboratory Medicine, Brown University, Providence, RI, USA, 02912.

7 George W. Woodruff School of Mechanical Engineering and Parker H. Petit Institute for Bioengineering and Bioscience, Georgia Institute of Technology, Atlanta, GA, USA, 30332

8 Wallace H Coulter Department of Biomedical Engineering, Georgia Institute of Technology, Atlanta, GA, USA 30332

Correspondence to: Erica Werner

Full address: Department of Cell Biology, Emory University. 615 Michael Street Room 455. Atlanta GA 30322. USA

E-mail: ewerner@emory.edu

Running title: Manganese induces mitochondrial dsRNA

Keywords: dsRNA; manganese; astrocyte; interferon.

Introduction

Manganese is an essential metal at trace levels, but neurotoxic in excess.[1] Manganese accumulates from environmental exposure, genetic defects, or secondary to liver damage.[2]

Contaminated water, air, and soil affect broad populations while miners, welders, and industrial workers are at high occupational exposure risk.[3-5] Mutations in manganese transporters controlling manganese influx (SLC39A14) or efflux (SL30A10) from cells and organisms increase brain and other organs levels leading to hypermanganesemia with dystonia 1 and 2 in humans.[6-8]

In the brain, manganese preferentially accumulates in the basal ganglia, causing manganism, which manifests as neuropsychiatric symptoms, and then progresses to dystonia and extrapyramidal dysfunction.[9,10] Chronic low level exposure increases the risk of cognitive, neuropsychiatric and behavioral symptoms in young and at-risk adult individuals.[5,11]

The mechanisms for manganese neurotoxicity remain poorly understood. Neuropathology of the globus pallidus in non-symptomatic and symptomatic individuals following manganese exposures, showed astrogliosis, increased glia and neuronal loss.[12-15] Microglia and astrocytes release cytokines at early and late stages of disease in manganese exposed mice, indicating a neuroinflammatory component to the pathogenic mechanism of toxicity in the brain.[16-20] Both glial cell types release cytokines in vitro,[21] with microglia-derived factors enhancing astrocyte responses.[22] These glial interactions exacerbate neuronal toxicity.[23,24] Neuroinflammation is a well-established response to injury, common to many neurodegenerative diseases and is proposed to be involved in both, disease initiation and progression.[25,26] The induction mechanisms for neuroinflammation have been proposed to be disease-specific. Here, we present a novel mechanism for the induction of neuroinflammation triggered by the generation of double stranded RNA (dsRNA) in mitochondria.

We previously showed that manganese disrupts processing of the mitochondrial transcriptome and induces accumulation of un-processed mitochondrial transcripts

intermediaries.[27] Processing of the mitochondrial polycistronic RNA is necessary to generate functional ribosomal, transfer, and messenger RNAs, which are required to synthetize thirteen mitochondrial-encoded respiratory chain proteins.[28] The bidirectional transcription of the mitochondrial DNA generates long complementary RNA which are homeostatically maintained by post-transcriptional modifications and degradation of non-coding transcripts.[29,30] Accumulation of complementary RNA has the potential to generate mitochondrial dsRNA, which exit mitochondria, activate cytosolic sensor molecules and trigger antiviral signaling pathways to produce type I interferon (IFN) responses.[31-33] We hypothesized that manganese-induced transcriptome defects are sufficient to induce inflammatory signaling. We demonstrate that sub-cytotoxic, manganese levels induce mitochondrial dsRNA, which triggers the IFN type I response and cytokine production in cell lines and in the most mature subpopulation of astrocytes in 100-day old human cerebral organoids. These findings are reproduced in vivo by the mouse brain of *Slc30a10* mutant mice, a genetic model of manganese accumulation. [34,35]

Materials and methods

Animals

The samples used in experiments shown in figure 6, were generously provided by Dr. Bartnikas. Punch biopsies from cortex and liver were obtained from wild type and *Slc30a10*$^{-/-}$ mice in C57BL/6N background as in [36] and were genotyped as in [6]. Mice were group housed in a standard 12 h light/dark cycle and were fed Rodent Diet 20 (cat# 5053, PicoLab) *ad libitum.* All animal care protocols and procedures were followed in accordance with NIH guidelines and with approval of Emory University's Institutional Animal Care and Use Committee.

Cell lines and media

HAP1 wild type and SLC30A10$^{-/-}$ cells were grown in Iscove's DMEM 10%FBS at 37ºC and 5%CO_2. HeLa cells were grown in DMEM 10%FBS 10mM Glutamine at 37ºC and 5%CO_2. Human iPSC A18945 were obtained through Emory Stem Cell and Organoids Core. iPSCs were cultured in feeder-free conditions, passaged using ReLeSR (Stem Cell Technologies) and cultured in StemFLex media (Thermo Fisher Scientific) at 37ºC and 5% CO_2. Astrocytes were differentiated and matured from neuroprogenitor cells employing StemCell differentiation and maturation media.

Cerebral organoids were developed as previously described.[37] On the first day, 18,000 cells were seeded for each organoid on 5-10 fiber scaffolds in low attachment plates. After 5 days, embryoid bodies were formed and transferred to induction media (Stem Cell Technologies) to direct them towards neuronal fate. After another 2 days, cells were expanded in Matrigel droplets for 3 days, then moved to organoid maturation media (Stem Cell Technologies). After 2 weeks in culture, the Matrigel was removed from the organoids by mechanical dissociation and the organoids were grown on an orbital shaker. Maturation media was changed twice a week during organoids growth for up to 100 days in culture.

Transfections and luciferase measurements

Stable cell lines were generated by transfection of HAP1 and HeLa cells with Lipofectamine 3000 (Invitrogen) and plasmid pNiFty3-L-Fluc-Puro followed by selection in media containing 5µg/ml Puromycin (Gibco). High Molecular weight Poly I:C was delivered at 1µg/ml by direct addition to the media at the time of Manganese treatment. The Sting agonist 2'3' cdAM(PS)2 (ADU-S100) was delivered by transfection with Lipofectamine 3000.

Following 24h treatment, the cells were washed with PBS, incubated with luciferase substrate Bright Glo (Promega) for 10 minutes at room temperature and luminescence measured in a white plate. SiRNA was delivered at 50nM by two sequential reverse transfections (at day 1 and 3) with RNAi-Max. Cells were treated at day 5 post-transfection and analyzed at day 6. Percentage of inhibition was calculated using as a reference the fold of change induced by manganese treatment in scrambled siRNA transfected cells.

Immunoblot

Cells were washed with PBS and lysed in 10 mM HEPES pH 7.4, 150 mM NaCl, 1 mM EGTA, and 0.1 mM MgCl2, with 0.5% Triton X-100 and Complete anti-protease. Proteins were separated by SDS-PAGE in 4-20% gels and transferred using the semidry transfer method to polyvinylidene difluoride membranes. Membranes were blocked in 5% nonfat milk and incubated overnight with primary antibody in 3% bovine serum albumin at 4ºC. Detection HRP labelled secondary was diluted 1:5000 and activity detected with Western Lightning Plus ECL substrate (PerkinElmer, NEL105001EA) and exposure to GE Healthcare Hyperfilm.

Immunofluorescence

Cells were fixed in 4% PFA at 37ºC for 20 minutes and permeabilized with 0.25% triton X100 on ice for 5 minutes. For dsRNA detection, permeabilization included 20U/ml SUPERase-In RNAse inhibitor. Control wells were treated with 5U/ml RNAseIII in PBS with 10mM $MgCl_2$ for 30 min at 37ºC in PBS. After blocking, primary antibodies were added: J2 1:300, GRSF1 1:500, Tom20 1:300, GFAP 1:300. Slides were imaged in a Nikon A1R HD25 confocal microscope with a 60x Apo lens (NA=1.4,WD=140uM). DsRNA localized to the mitochondrial granule positive for GSRF1 was quantified with Image J/Fiji software in the focal plane of maximal intensity of a Z-stack. On both images, background

was subtracted with a 30 radius and segmented by thresholding. Measurements of fluorescence of dsRNA per cell were directed and limited to the corresponding GSRF1 image. At least 30 cells in a minimum of 5 fields were measured. Organoids were fixed overnight in 4%PFA and then incubated in sucrose before embedding. 8µm paraffin sections were re-hydrated by alcohol dilution series washes and antigen retrieval was performed for 20 min in Citrate buffer pH6 with 0.05% Tween at 60% power in the microwave and then stained as described above. Organoid images were corrected by brightness and contrast to distinguish positive from negative cells and background signal. Cells within 300µm from the organoid surface, in 5 different captured fields were identified as GFAP positive and classified as dsRNA positive or negative. Identical scoring was obtained by two independent observers.

Cytokine measurements

Human Cytokine Array was used to profile cytokines in conditioned media following 48h manganese treatment in HeLa (750µM) and Hap1(150µM) cells. A high and a low exposure film was quantified by thresholding and measuring the signal intensity with the circular brush selection in FIJI/Image J on each spot and an equal adjacent area to subtract local background. CXCL8/IL8 was measured in media conditioned for 48h employing Elisa assays following manufacturer's protocols. The human Proinflammatory 9-Plex panel from MesoScale and R-PLEX Human B2M Antibody Set were employed to measure cytokines and beta 2 microglobulin in conditioned media from organoid treated for 48h by the Emory Multiplexed Immunoassay Core.

Cell survival assay

Cells were plated at 2,000 cells/well the day before drugs were added. Cells were treated with the drug concentrations indicated for 72 h and 10% Resazurin in media was incubated for 2 hours at 37ºC.Fluorescence was measured in a microplate reader (BioTek Synergy HT). Percent survival was calculated by subtracting the background of Alamar blue and normalizing to the untreated condition for each genotype. Individual data points represent the average survival of triplicate treatments for each concentration.

RNA extraction and NanoString mRNA quantification

Cells were solubilized in 1 ml of TRIzol (Invitrogen). RNA Extraction and NanoString processing was done by the Emory Integrated Genomics Core. RNA quality was assessed by bioanalyzer. mRNA counts were normalized to housekeeping genes TBP for the neuroinflammatory panel and CLCT for the MitoString using nSolver. Normalized data were further processed and visualized in Qlucore.

Cytokine/Chemokine Multiplex Luminex Immunoassay

Frozen mouse brain samples were provided by Dr. Tom Bartnikas. Shavings of frozen tissue were lysed in 8M urea in 100mM PO_4 with Complete anti-protease and PhosSTOP phosphatase inhibitor and homogenized by sonication (Fisher Scientific, Sonic Dismembrator Model 100). Protein concentration was measured in triplicate using the Pierce BCA Protein Assay Kit (Thermo Fisher Scientific). 5 µg of brain and 15 µg of liver tissue samples were diluted using urea buffer and analyzed using the Milliplex MAP Mouse Cytokine/Chemokine Multiplex assay Eotaxin/CCL11, G-CSF, GM-CSF, IFN-γ, IL-1α, IL-1β, IL-2, IL-3, IL-4, IL-5, IL-6, IL-7, IL-9, IL-10, IL-12 (p40), IL-12 (p70), IL-13, IL-15, IL-17, IP-10, KC, LIF, LIX, MCP-1, M-CSF, MIG, MIP-1α, MIP-1β, MIP-2, RANTES, TNF-α, VEGF. Assays were read out with a MAGPIX Luminex instrument (Luminex, Austin, TX, USA).

Inductively Coupled Plasma Mass Spectrometry

Procedures were described previously.[38] Briefly, cells were detached with trypsin, pelleted at 800 × g for 5 min at 4Cº and digested by adding 50 µL of 70% trace metal basis grade nitric acid with heating at 95ºC for 10 min. Metal levels were quantified with a triple quad ICP-MS instrument (Thermo Fisher, iCAP-TQ) operating in oxygen mode under standard conditions (RF power 1550 W, sample depth 5.0 mm, nebulizer flow 1.12L/min, spray chamber 3C, extraction lens 1,2 -195, –-15 V). Oxygen was used as reaction gas at 0.3 mL/min to remove polyatomic interferences and mass shift target elements. External calibration curves ranging from 0.5 to 1000 µg/L were generated for each element with a multielemental standard (ICP-MSCAL2-1, AccuStandard, USA). Scandium (10 µg/L) was used as internal standard diluted into the sample in-line. Samples were introduced into the ICP-MS using the 2DX PrepFAST M5 autosampler (Elemental Scientific) equipped with a 250 µL loop and using the 0.25 mL precision method following manufacturer recommendations. Serumnorm (Sero, Norway) was used as a standard reference material, yielding values for elements of interest within 20% of the accepted value. Quantitative data analysis was conducted with Qtegra software.

Cell isolation and capture for scRNAseq

Organoids were dissociated into a single cell suspension using previously published methods [39] adapted for organoids dissociation by decreasing volumes and omission of filtering steps. Briefly, organoid tissue was chopped using a scalpel and digested in 10ml with 25 U/ml papain (Worthington) and 12.5 U/ml DNAseI (Worthington) in a 5% CO2 incubator at 34ºC on an orbital shaker at 123rpm for 45 min. Cells were washed with a protease inhibitor solution (ovomucoid). Following addition of Ovomucoid, the tissue was further triturated by pipetting and once single cell suspensions achieved, the cells were collected by centrifugation. All dissociation and trituration steps were performed in the presence of

Protector RNAse inhibitor, transcription inhibitor actinomycin D, and translation inhibitor anisomycin based on published recommendations [40]. Up to 10,000 cells per organoid were captured with a Chromium GEM-X-Single Cell 3' Chip kit v4 from 10X Genomics. Libraries were prepared using Chromium Next GEM Single Cell 3' Kit v4 with dual index labeling and sequenced on a standard Illumina platform.

Single cell sequencing analysis

The sequencing data were aligned to the human genome and demultiplexed using Cellranger. Analysis was performed in R Studio using Seurat. For quality control, cells with <8% mitochondrial genes were excluded, and counts were filtered for 500-8000 range. Cells were integrated and normalized using SCT transform to generate a UMAP and clustering based on based on shared nearest neighbors. All featureplots, dot plots, and differential expression are based on non-transformed RNA counts. Differential expression was performed using pseudobulk data aggregation and Findmarkers DeSEQ2. Heatmaps are based in scaled RNA counts data.

Statistical analysis

NanoString data was normalized with nCounter and then processed with Qlucore Omics Explorer Version 3.6 Software. ANOVA and paired analyses were conducted with Prism Version 10.2.2. Gene ontology studies were performed with ENRICHR [41].

Luminex Cytokine Statistical and Multivariate Analyses, Wilcoxon rank sum test was performed in R. Partial least squares regressions (PLSRs) and discriminant PLSRs (D-PLSRs) were performed in R using the *ropls* package v1.4.2. The data were z-scored before being input into the function. Cytokine measurements were used as the independent variables, and the discrete regression variable in all D-PLSR analyses was genotype/sex. Error bars for

LV loadings were calculated by iteratively excluding K samples without replacement 100 times (leave-K-out cross-validation, LKOCV) and regenerating the D-PLSR model each time. Error bars in the LV1 plots report the mean and SD computed across the models generated to provide an indication of the variability within each cytokine among the models generated.

Data availability

We provide access to Datasets with the data used to generate figures in the manuscript with a DOI of the preprint of this manuscript. We will upload the raw sequencing file of the scRNAseq experiment to Gene Expression Omnibus Database. and provide an access number. At this time, we will generate a GitHub page to post code generated for the analysis referenced by a DOI generated with the Zenodo tool.

Results

Exposure to manganese leads to the accumulation of mitochondrial dsRNA

We previously found that manganese alters mitochondrial RNA processing, measured by molecular counting employing a custom NanoString panel designed to detect mitochondrial mRNA, tRNA-mRNA, and tRNA-rRNA junctions as well as non-coding regions in the polycistronic RNA arising from the transcription of both, the H and L strand of mtDNA.[27,42] On close analysis, we observed the accumulation of non-coding RNA sequences of the L strand transcript, sequences that are normally degraded,[30,31] in HAP1 SLC30A10$^{-/-}$cells as well as HAP1 and HeLa cells treated for 24h with manganese at 300 and 800µM respectively (Fig. 1A). In contrast, transcripts levels for TFAM, SDHA, or POLMRT did not change consistently, indicating no change in mitochondrial mass. Linear and non-linear dimensionality reduction of the data by principal component analysis and by Uniform

Manifold Approximation and Projection (UMAP, insert), demonstrated clustering of all the control samples and segregating away from all samples with increased manganese resulting from either manganese exposure or mutagenesis of the SLC30A10 efflux transporter (Fig. 1B). The alterations of the mitochondrial transcriptome after manganese exposure of wild-type cells occur at IC_{50} metal doses (50% death when survival was measured at day 3 post-Mn treatment,[27] Fig. 3E and Supplementary Fig. 3C). These treatment doses resulted in a cellular manganese accumulation, reflected by the Mn/P ratio, comparable to the observed in brain cortex and liver of *Slc30a10*$^{-/-}$ mice, which accumulate manganese from the diet over time in a sex-independent manner, as has been previously reported (Fig. 1C, top panel).[6] Both treatment doses lead to a 50-fold increase in manganese content in each cell type, comparable to liver of *Slc30a10*$^{-/-}$ mice (Fig.1C bottom panel), without changing the content of Fe, Zn and Ca in cells and brain (Supplementary Fig. 1).

We reasoned that the dysregulated persistence of RNA transcripts of complementary sequence belonging to the H and L-strands could lead to dsRNA accumulation in mitochondria. We tested this hypothesis by detecting dsRNA co-localization with the mitochondrial RNA granule component GRSF1 by immunofluorescence with the J2 antibody, a monoclonal antibody that binds to dsRNA molecules larger than 40bp irrespective of sequence (Fig. 1D). [43] Both cell lines showed increased levels of dsRNA in mitochondria following 24h manganese treatment. dsRNA immunoreactivity was downregulated by inhibition of the mitochondrial RNA polymerase POLRMT with IMT1,[44] indicating that the mitochondrial origin of the dsRNA signal induced by manganese is mitochondrial transcription (Fig. 1E). RNAse III was used as a specificity control to degrade dsRNA prior to immune labeling (Fig. 1E).

Manganese induced dsRNA activate type I Interferon responses

dsRNA of mitochondrial origin are known to escape from mitochondria into the cytoplasm where they are recognized by the dsRNA receptors, retinoic acid inducible gene 1 (RIG-1) and melanoma differentiation-associated protein 5 (MDA5).[32] Once bound to dsRNA, these receptors are recruited to a multiprotein aggregate comprised of MAVS and signaling proteins. This multiprotein assembly activates the kinase TBK1, which phosphorylates IRF3, enabling its nuclear translocation to induce IFNβ transcription thereby activating a cascade of interferon-stimulated genes (ISGs) (Fig. 2A).[32,45] To test the activation of this dsRNA receptor pathway by manganese, we expressed a reporter construct in which the IFNβ promoter drives luciferase expression. While HAP1 cells accumulated significant levels of dsRNA in mitochondria (Fig. 1D and E), no manganese concentration induced luciferase expression in these cells (Fig. 2B). This outcome suggests that dsRNA is retained in mitochondria in HAP1 cells, because the pathway was readily triggered by delivery of the membrane-permeable synthetic dsRNA agonist, poly(I:C) (Fig. 2B). In contrast, sub-IC_{50} manganese doses were sufficient to increase luciferase activity up to four-fold in HeLa cells (Fig. 2B). We next identified the receptor that recognizes manganese-induced mitochondrial dsRNA in the cytosol by knockdown experiments. Reduced expression of MDA5, but not RIG-1, downregulated manganese-induced luciferase activity by 40% (± 11% SEM) (Fig. 2C). Combination knockdown of RIG-1 and MDA5 did not change the inhibitory effect of MDA5 downregulation, indicating that of the two dsRNA receptors, only MDA5 is required to recognize manganese-induced dsRNA. In contrast, RIG-1 was the receptor for poly(I:C) (Fig. 2C). We further confirmed mitochondrial dsRNA signaling by pharmacological inhibition of predicted components in the pathway (Fig. 2A and D). Interferon promoter transcription was reduced by downregulating mitochondrial transcription with the inhibitor IMT1, which targets the mitochondrial RNA polymerase (POLRMT). Interferon promoter transcription was also reduced by interfering with dsRNA export to the cytosol by either

inhibiting the permeability transition pore function in the inner mitochondrial membrane with cyclosporine A (CspA) or by blocking the Bax-Bak mitochondrial pore in the outer mitochondrial membrane with V5 peptide (Fig. 2A).[46-48] None of these inhibitors reduced manganese uptake by cells (Fig. 2D top panel) but all reduced IFNβ transcription by at least 25%, with 100% decrease when TBK1 was inhibited with GSK8612 (Fig. 2D bottom panel). Another potent activator of the antiviral pathway is the release of mitochondrial DNA (mtDNA) into the cytosol which activates the cGAS-STING converging to TBK1 activation (Fig. 2A). We excluded a contribution of mtDNA to signaling by pharmacological inhibition of STING with H151, which did not affect manganese or poly(I:C) induced luciferase transcription (Fig. 2E). H151 effectively blocked STING activation-induced transcription by the agonist 2'3 c-di-AM$(PS)_2$ Rp,Rp (ADU S100) (Fig. 2E). Taken together, these results indicate that manganese increases dsRNA in mitochondria of both cell lines, but dsRNA reach the cytoplasm where they bind to MDA5 and lead to increased IFNβ transcription only in HeLa cells.

Manganese-induced accumulation of mitochondrial dsRNA results in neuroinflammatory responses

Next, we asked whether IFNβ transcriptional activation occurs in the context of a broader inflammatory response by profiling conditioned media of HAP1 and HeLa cells following a 48h manganese exposure with a cytokine profiling antibody array (Fig. 3A). While no significant changes were detected in HAP1 cells (Supplementary Fig. 3B), we identified several cytokines and chemokines induced in response to increased manganese concentration in HeLa cells (Figs. 3A and B, Supplementary Fig. 3A). Notably, the chemokines CXCL10 and GM-CSF were robustly upregulated by manganese, both of which have been shown to be upregulated following poly (I:C) treatment of epithelial cells.[49] We detected modest increases

in IL8, but not IL6, in the cytokine array which we confirmed by ELISA assay (Fig. 3C and D). We focused on IL8 production to monitor manganese-induced inflammatory responses as this cytokine is responsive to both interferon and NFκB activation by indirect and direct mechanisms, respectively and all cell types in the brain express receptors for this chemokine [50].

Manganese induced IL8 expression following 48h treatment with a sub-IC_{50} manganese dose (Fig. 3C and E). This upregulation was reduced by inhibition of the mitochondrial RNA polymerase POLRMT with IMT1, the Bax-Bak pore function with V5 peptide, or a TBK1 inhibitor (Fig 3D). Importantly, none of the inhibitors affected cell survival of either cell line in response to manganese, which suggests that the inflammatory responses induced by dsRNA do not play a role in cytotoxicity (Fig. 3E, Supplementary Fig. 3C). Addition of the pan-caspase inhibitor Q-VD-Oph reduced cytotoxicity in HAP1 cells (Supplementary Fig. 3C) but did not affect HeLa survival, indicating that no apoptotic mechanisms play a role in this inflammatory response either (Fig. 3E, Supplementary Fig. 3C).

To gain further understanding of how manganese cytotoxicity and inflammation take place in a model system for brain tissue, we studied the effects of manganese on the mitochondrial transcriptome and cytokine secretion in human iPSC-derived cerebral organoids. We chose the unguided method for organoid growth as it provides diversified cell types and developmental paths to interrogate.[37] To select the appropriate developmental timepoint to analyze, we tested for processing of mitochondrial transcripts over organoid development time with the MitoString panel, which we customized by adding probes to monitor differentiation of neuroprogenitor cells (NPC), neurons, and astrocytes. We found that neuroprogenitor cell markers declined overtime from Day 30 on, with a steady increase in neuron maturation and astrocyte markers at Days 60 and 100 (Fig 4A and B). These transcriptional differentiation responses occurred concomitantly with morphological

maturation and layering of the organoids as determined by confocal immunomicroscopy with antibodies against the cortical layer markers Ctip2 and Satb2 and by the progressive loss of immunoreactivity of the neuroprogenitor marker Sox2 (Supplementary Fig. 4A).

The organoids were treated with manganese for 48h at several times of their development. After treatment organoids were collected for RNA analysis and conditioned media for cytokine measurement. We used a dose of 250μM manganese, a concentration that is approximately equivalent to the metal concentrations estimated to accumulate in the striatum and globus pallidus of manganese-exposed primate and rodent models.[51] Using this strategy, we found that Day 30- and 60 organoids did not show significant changes in mitochondrial-encoded RNAs or levels of their processing intermediaries. However, we found robust changes in Day 100 organoids, including increases of most of the mitochondrial-encoded mRNA, some tRNA-mRNA junctions and several non-coding RNA encoded in the L strand of the mitochondrial genome (Fig. 4C). These modifications of the mitochondrial transcriptome occurred without changes in the nuclear-encoded mitochondrial genes TFAM, POLG, and POLRMT, excluding increases in mitochondrial content in Day 100 organoids after 48h of manganese exposure.

We comprehensively interrogated the bulk 100-day organoid transcriptome to characterize the inflammatory responses induced by manganese employing the Neuroinflammatory (Fig. 4D and E) and Neuropathology (Supplementary Fig. 3B and C) panels from NanoString. Hybridization with the Neuroinflammatory panel demonstrated upregulation of multiple inflammation-annotated mRNAs as represented in a volcano plot (Fig. 4D). Several genes that are transcriptional targets of IRF3 and NFκB as well as interferon stimulated genes (ISG) were significantly upregulated after manganese exposure (Fig. 4E). We measured secretion of inflammatory cytokines by analyzing the presence of IL6 and IL8 in conditioned organoid media with Mesoscale ELISA assays. Manganese

significantly increased IL8 levels in conditioned media of organoids exposed to 250μM dose in two independent organoid cohorts (Fig. 4F, Supplementary Fig. 4D). We observed a fraction of organoids with higher levels of basal cytokine secretion in the absence of manganese treatment (Fig. 4F, Supplementary Fig. 4D). Basal untreated and manganese-induced cytokine secretion levels remained unaltered after normalizing organelle secretory activity and size by beta-2 microglobulin, a protein constitutively expressed and secreted by all cells (Fig. 4F). Analysis of the Neuropathology panel demonstrated that at this time of development and manganese concentration, there were no changes in the expression of transcripts annotated to either neurons and astrocytes or associated with disease mechanisms such as hypoxia, the unfolded protein response, or NRF2-dependent pathway signaling (Supplementary Fig. 4C). Taken together, these results indicate that the manganese-induced mitochondrial and interferon type 1 inflammatory responses are present in brain cell types and are not part of an overt stress or cytotoxic response in brain organoids that lack microglia.

Manganese induces inflammatory responses in astrocytes

To identify the cell types engaged in inflammatory responses to manganese in the organoids, we performed 10x scRNAseq on 12 individual organoids. Six organoids were left untreated and six were exposed to 250μM manganese for 48h. A total of 119,996 cells were analyzed and clustered into 8 distinct cell populations, including proliferative, fibroblast, choroid plexus, radial glia, astrocyte, neural progenitor, and two neuronal categories (Fig. 5A, QC metrics in Supplementary Fig. 5A). All cell populations were proportionally present in all 12 organoids regardless of organoid size and manganese treatment (Fig. 5B, Supplementary Fig. 5C). Cell clusters were manually identified based on differential gene expression profiles (Fig. 5C) and were of restricted expression as demonstrated by Feature Plots (Supplementary Fig. 5B). Manganese did not preferentially affect the cell count in any specific cluster

(Supplementary Fig. 5D) We also examined the expression of selected inflammatory genes and identified astrocytes as the major cell population driving inflammatory responses in the organoids following manganese treatment (Fig. 5C). To gain insights into the mechanisms and molecular phenotypes elicited by manganese treatment in astrocytes, we obtained the differentially expressed genes via pseudobulking and DESeq2 to compare control and treated organoids (Fig. 5D), then conducted gene ontology analysis (Fig. 5E). Significantly up- and down regulated genes are represented in a volcano plot, where we highlight genes relevant to astrocyte function, CXCL10 and selected genes annotated to the pathways identified in bioinformatic analysis (Fig. 5D). Transcripts upregulated by manganese were enriched in genes annotated to interferon alpha responses, cholesterol biosynthesis and oxidative phosphorylation pathways in the MSigDB Hallmark 2020 database.[52] Downregulated transcripts were annotated to UV response, hypoxia and TGFβ signaling (Fig. 5E). These manganese-induced responses were elicited across the treated individual organoids (Fig. 5F). Manganese increased the expression of CXCL8 and CXCL10, mitochondrial genes, subunits of the respiratory chain, and interferon response genes. Genes induced by manganese correlated with higher mRNA levels of astrocytic reactivity markers, cholesterol synthesis, and neuron supporting genes, but lower levels of transcripts annotated to phagocytosis. Feature maps of CXCL8 and CXCL10 expression revealed that a subpopulation of astrocytes expressed these chemokines, suggesting heterogeneity among the astrocyte responses (Fig. 5G). To characterize and identify unique attributes of these chemokine-expressing astrocytes, we subclustered astrocytes into 3 sub-populations (Fig. 5H, Astro 1,2 and 3), where Astro 2 concentrated the cytokine expressing cells (Fig. 5I). Comparison of the differentially expressed genes in response to manganese showed that Astro 2 cluster also concentrated cells with the most robust induction of the interferon response genes, accumulated mitochondrial-encoded transcripts, and displayed reduced expression of HSD17B10 and REXO2.

HSD17B10 is a component of the mitochondrial RNA processing complex RNaseP [53] and REXO2 participates in mitochondrial dsRNA degradation (Fig. 5I and Supplementary Dataset S8).[54] The heterogeneous astrocyte responses detected by scRNAseq was also evident by immunomicroscopy of manganese-treated organoids stained for dsRNA and GFAP (Fig. 5J-1). We found that 36% of GFAP-positive astrocytes were also positive for dsRNA after exposing organoids to manganese (Fig 5J-2). We confirmed that dsRNA signal colocalized with mitochondrial markers in iPSC-derived astrocytes exposed to the same manganese challenge as organoids (Fig. 5J-3).

Chronic increased manganese induces inflammation in brain and liver in vivo

While organoids are an in vitro model for brain tissue well-suited to perform dose- and time-controlled experiments of acute manganese exposures, we asked next whether inflammatory responses and the activation of type 1 interferon responses are part of the phenotype following chronic excess manganese accumulation in brain tissue in vivo. Mice with a global deficiency in the manganese efflux pump Slc30a10 progressively accumulate manganese in the brain from the diet.[6] At eight weeks of postnatal age, *Slc30a10*$^{-/-}$ mice reproduce several of the phenotypes observed in the human SLC30A10 genetic disease hypermanganesemia with dystonia 1 disorder (OMIM 613280), including motor deficits.[6] We measured the expression levels of 32 cytokines in brain and liver samples from wild type and *Slc30a10*$^{-/-}$ mice of both sexes as we have done before.[55] We included liver as this organ is one of the tissues with the highest levels of manganese accumulation (Fig.1C).[6] We found a complex pattern of altered cytokine expression modulated by sex, with higher expression levels of cytokines in KO tissues in both organs (Figs. 6A and Supplementary Fig. 6A). To resolve cytokines whose expression was strongly associated with the mutant genotype, we

analyzed these data by discriminant partial least squares regression analysis, which enables us to study these multivariate datasets by reducing data from 32 measured variables to a reduced set of latent variables (LV1 and LV2) (Figs. 6B and Supplementary Fig. 5B). Reducing the dataset to these latent variables allowed us to identify differences between genotypes distinguishing cytokine changes correlated with genotype from unrelated noise in the measurements.[55,56] Each LV represents a profile of cytokines that vary together between wild type and KO animals. We found that LV1 distinguished wild type animals and KO animals, irrespective of sex (Figs. 6B and Supplementary Fig.6B, *x* axis). We used a leave-one-out cross validation strategy, wherein each animal was iteratively left out, and the discriminant partial least squares regression analysis was re-computed. We found low standard deviation in each cytokine, suggesting that the involvement of each cytokine is not dependent on any single tissue sample (Figs. 6B and Supplementary Fig. 6B). Moreover, the cytokine expression pattern was different in cortical and liver samples. In brain, some of the upregulated cytokines are known to be produced by astrocytes,[57]while Vegf, a cytokine responsive to hypoxia, was elevated in liver but not in cortex of KO animals, reproducing previous RNAseq findings.[58] In contrast, IL12b, was increased in both mutant tissues. (Figs. 6B and Supplementary Fig. 6B). We profiled the wild type and *Slc30a10*$^{-/-}$ brain transcriptomes using a NanoString panel with 770 probes enriched for neuroinflammatory genes and glial reactivity. Seventy-two genes were significantly upregulated when comparing wild type and knockout animals of both sexes combined (Fig. 6D, $p<0.05$ and fold change >1.5, Dataset S9) with C3 and markers of the ISG among the most upregulated. The transcriptome alterations and in cytokines profiles in female mutant brain were attenuated compared to the male brains (Fig. 6E and F), however all mice exhibited upregulated interferon response and markers of reactive astrocytes and microglia (Fig. 6G). Altogether,

these results demonstrate the sustained expression of inflammatory responses with activation of type1 interferon responses in *Slc30a10*$^{-/-}$ brain tissues.

Discussion

We identified a novel mechanism by which manganese induces inflammatory responses in non-immune cells, initiated by altered mitochondrial transcriptome processing that activates anti-viral type I interferon responses and inflammatory cytokines. Manganese causes dsRNA accumulation in mitochondria, detected by localization to the mitochondrial RNA granule and by accumulation of unprocessed non-coding segments of mitochondrial transcripts in multiple cell types, including HeLa, HAP1, and cerebral organoids astrocytes. Pharmacological and genetic interventions confirmed that mitochondrial dsRNA drives pro-inflammatory signaling. IFNβ transcription and IL8 production were reduced by blocking mitochondrial transcription with the mitochondrial RNA polymerase inhibitor IMT1 or dsRNA export to the cytosol with inhibitors targeting mitochondrial membrane permeability. We identified MDA5 as a cytoplasmic receptor sensing dsRNA, signaling to TBK1. Inhibitors or protein knockdowns targeting components of the pathway upstream of TBK1 activation, partially reduced responses but TBK1 inhibitors were highly effective, suggesting that manganese activates TBK1 through additional mechanism, possibly by binding to PKR or modulating ATM activity. [59-61] Nonetheless, TBK1 inhibitors strongly downregulated IFNβ and IL8, showing that dsRNA drives inflammation but not cell death.

We observed activation of type 1 interferon responses across complementary experimental models. Acute manganese exposure in cell lines and cerebral organoids produced phenotypes also seen in *Slc30a10*$^{-/-}$ mouse brains, at an age when they show overt motor symptoms, indicating that these interferon responses may contribute to pathogenesis.[8] Phenotypic overlap across models validated manganese doses and mechanisms. Because

human brain manganese levels following exposures or in hypermanganesemia with dystonia 1 disease are not known, relevant exposure doses are inferred from animal model exposures, plasma levels after human exposure and findings in hepatic encephalopathy.[62,63] We argue that an important parameter to identify disease mechanisms is the intracellular manganese levels, defined by uptake, organelle accumulation and efflux, which is the critical determinant of downstream signaling. We provide support for this premise by comparing the relative enrichment expressed as the manganese to phosphate ratio attained in acutely exposed cells, which matched the ratios in brain and liver of *Slc30a10*$^{-/-}$ mice. Importantly, because manganese content of tissues represent the average of multiple cell types, it may be possible that some cell types in *Slc30a10*$^{-/-}$ tissues may reach higher levels of manganese as the ones we report here.

Cerebral organoids modeled human astrocyte and neuron responses to manganese during development, in the absence of contributions to inflammation from microglia, immune cells and blood vessels, which may affect in vivo outcomes. We show that changes in mitochondrial RNA transcript processing and inflammatory responses emerge during astrocyte maturation. Both, single cell RNAseq and bulk RNA transcriptomes analyses of organoids exposed to a short and non-lethal manganese treatment identified a small sub population of astrocytes as the main cell type driving IL-8 and CXCL10 expression/secretion and the induction of interferon response genes. Immunofluorescence confirmed that some GFAP-positive astrocytes accumulated dsRNA. These findings align with large single cell RNAseq studies in mice showing astrocyte heterogeneity across brain regions and in their capacity to respond to pro-inflammatory stimuli, including LPS and pro-inflammatory cytokines.[64,65]

The transcriptional signature of these reactive astrocytes in organoids shows a combination of deleterious markers such as reduced phagocytosis and high C3 expression,

co-expressed with neuron-supporting phenotypes, such as cholesterol biosynthesis, cytoskeleton genes controlling cell area, and glutamate transporters. Multiple genes of this complex astrocyte signature were upregulated in *Slc30a10*$^{-/-}$ mice cortical tissue indicating the presence of these mechanisms in the mouse model. In brain cortex, we detected upregulated microglial markers, however they did not fully overlap with a specific reactivity phenotype such as Disease Associated Microglia (DAM), defined by downregulation of homeostatic genes *Cx3cr1*, *Tmem119* and *P2y12* with upregulation of *Trem2* and *Tyrodp*.[66,67] Altogether, our findings implicate astrocytes as a primary manganese target in vitro and in vivo.

We show that type I interferon responses are triggered within 24-48h of manganese exposure. Our findings are supported by published transcriptome datasets, which reveal manganese-dependent induction of interferon responses in human fetal astrocytes treated for 7-days in vitro.[68] Bulk RNA transcriptomic studies in *Slc30a10*$^{-/-}$ mice showed upregulation of GFAP, CXCL10 and the interferon response genes Oas2 and 3 in brain, but not in liver.[69] When basal ganglia of 1 month old *Slc30a10*$^{-/-}$ mice were analyzed by bulk RNAseq, interferon responses were one of the major categories of genes upregulated in 2 of the 3 regions probed and could be reversed by lowering dietary manganese.[70] Because astrocytes exhibit high manganese uptake and persistent activation into adulthood when mice are exposed as juveniles,[71] transient exposures may trigger lasting interferon responses. All brain cells express IFNβ receptors, and a basal tone is essential for development and cognition.[72,73] Low astrocytic IFNβ promotes synaptic spine formation and cognitive function in hippocampus [74] and primes microglia phagocytic activity towards neuronal bodies early in development.[75] Complete absence of this pathway or excess is pathogenic. For example, IFNβ or IFNR loss of function is sufficient to cause Parkinson's- like neurodegeneration.[76] Excess Interferon signaling is associated with Dystonia in Aicardi Goutieres syndrome [77] and

secondary to Type I IFN therapy.[72,78] Cytokines from manganese-exposed astrocytes may therefore mediate cognitive and behavioral symptoms.

Mitochondrial nucleic acids are emerging inflammatory triggers. While mtDNA has been implicated in neurodegeneration,[79] less is currently known about RNA from this organelle. Increased mitochondrial RNA has been found in the cytoplasm of neurons in mouse models of Huntington disease [80] and senescence.[81] We propose mitochondrial dsRNA-dependent signaling as a general mechanism for triggering adaptive and maladaptive inflammation in diverse neurodegenerative disorders. CRISPR screens implicate mitochondrial enzymes in RNA processing and dsRNA accumulation.[42,82] Cellular metabolism influences RNA processing. Hypoxia supresses mitochondrial transcription and interferon signaling in cancer cell lines.[47,83] Metabolites generated by the mitochondrial enzymes fumarate hydratase [84] and aconitate decarboxylase, itaconate [85] promote dsRNA accumulation and inflammatory responses. Thus, the mitochondrial transcriptome is both a target and an effector of manganese-induced signaling.

Acknowledgements

Research reported in this publication was supported in part by Emory University subsidized cores: Emory Integrated Genomics Core (EIGC, RRID# iSCR_023529), Emory Multiplexed Immunoassay Core (EMIC), Emory Stem Cell and Organoids Core (ESCOC RRID# SCR_023264), Integrated Cellular Imaging (ICI, RRID:SCR_023534) of the Winship Cancer Institute of Emory University and NIH/NCI under award number, 2P30CA138292-04.

Funding

This work was supported by NIH grant R01ES034796 to EW and AG, Udall Center Pilot Project Grants for Parkinson's Disease Research to AG, Hercules Pilot Award NIEHS P30ES019776 to EW and AG, Cure Alzheimer's Fund grant to VF, NIH T32NS096050 to HM-V, NIH K00 ES033033 and BWF PDEP to MMS, NIMH R01 MH125956 to SAS, 1R01AG075820 to LBW, FGRM was funded in part by the Cell and Tissue Engineering Training Grant NIH T32GM145735 NIGMS, NIH R01 DK110049 to TBB.

Competing interests

The authors report no competing interests.

Supplementary material

Supplementary material is available at *Brain* online.

References

1. Balachandran RC, Mukhopadhyay S, McBride D, et al. Brain manganese and the balance between essential roles and neurotoxicity. *J Biol Chem*. May 8 2020;295(19):6312-6329. doi:10.1074/jbc.REV119.009453
2. Peres TV, Schettinger MR, Chen P, et al. "Manganese-induced neurotoxicity: a review of its behavioral consequences and neuroprotective strategies". *BMC Pharmacol Toxicol*. Nov 4 2016;17(1):57. doi:10.1186/s40360-016-0099-0
3. Lucas EL, Bertrand P, Guazzetti S, et al. Impact of ferromanganese alloy plants on household dust manganese levels: implications for childhood exposure. *Environ Res*. Apr 2015;138:279-90. doi:10.1016/j.envres.2015.01.019
4. Kornblith ES, Casey SL, Lobdell DT, Colledge MA, Bowler RM. Environmental exposure to manganese in air: Tremor, motor and cognitive symptom profiles. *Neurotoxicology*. Jan 2018;64:152-158. doi:10.1016/j.neuro.2017.09.012
5. Schullehner J, Thygesen M, Kristiansen SM, Hansen B, Pedersen CB, Dalsgaard S. Exposure to Manganese in Drinking Water during Childhood and Association with Attention-Deficit Hyperactivity Disorder: A Nationwide Cohort Study. *Environ Health Perspect*. Sep 2020;128(9):97004. doi:10.1289/EHP6391

6. Mercadante CJ, Prajapati M, Conboy HL, et al. Manganese transporter Slc30a10 controls physiological manganese excretion and toxicity. *J Clin Invest*. Dec 2 2019;129(12):5442-5461. doi:10.1172/JCI129710
7. Rodichkin AN, Guilarte TR. Hereditary Disorders of Manganese Metabolism: Pathophysiology of Childhood-Onset Dystonia-Parkinsonism in SLC39A14 Mutation Carriers and Genetic Animal Models. *Int J Mol Sci*. Oct 24 2022;23(21)doi:10.3390/ijms232112833
8. Taylor CA, Hutchens S, Liu C, et al. SLC30A10 transporter in the digestive system regulates brain manganese under basal conditions while brain SLC30A10 protects against neurotoxicity. *J Biol Chem*. Feb 8 2019;294(6):1860-1876. doi:10.1074/jbc.RA118.005628
9. Lucchini R, Apostoli P, Perrone C, et al. Long-term exposure to "low levels" of manganese oxides and neurofunctional changes in ferroalloy workers. *Neurotoxicology*. Apr-Jun 1999;20(2-3):287-97.
10. Anagianni S, Tuschl K. Genetic Disorders of Manganese Metabolism. *Curr Neurol Neurosci Rep*. May 14 2019;19(6):33. doi:10.1007/s11910-019-0942-y
11. Mergler D, Baldwin M, Belanger S, et al. Manganese neurotoxicity, a continuum of dysfunction: results from a community based study. *Neurotoxicology*. Apr-Jun 1999;20(2-3):327-42.
12. Olanow CW. Manganese-induced parkinsonism and Parkinson's disease. *Ann N Y Acad Sci*. Mar 2004;1012:209-23. doi:10.1196/annals.1306.018
13. Perl DP, Olanow CW. The neuropathology of manganese-induced Parkinsonism. *J Neuropathol Exp Neurol*. Aug 2007;66(8):675-82. doi:10.1097/nen.0b013e31812503cf
14. Gonzalez-Cuyar LF, Nelson G, Criswell SR, et al. Quantitative neuropathology associated with chronic manganese exposure in South African mine workers. *Neurotoxicology*. Dec 2014;45:260-6. doi:10.1016/j.neuro.2013.12.008
15. Vezer T, Kurunczi A, Naray M, Papp A, Nagymajtenyi L. Behavioral effects of subchronic inorganic manganese exposure in rats. *Am J Ind Med*. Nov 2007;50(11):841-52. doi:10.1002/ajim.20485
16. Antonini JM, Sriram K, Benkovic SA, et al. Mild steel welding fume causes manganese accumulation and subtle neuroinflammatory changes but not overt neuronal damage in discrete brain regions of rats after short-term inhalation exposure. *Neurotoxicology*. Nov 2009;30(6):915-25. doi:10.1016/j.neuro.2009.09.006
17. Filipov NM, Dodd CA. Role of glial cells in manganese neurotoxicity. *J Appl Toxicol*. May 2012;32(5):310-7. doi:10.1002/jat.1762
18. Tjalkens RB, Popichak KA, Kirkley KA. Inflammatory Activation of Microglia and Astrocytes in Manganese Neurotoxicity. *Adv Neurobiol*. 2017;18:159-181. doi:10.1007/978-3-319-60189-2_8
19. Fan XM, Luo Y, Cao YM, et al. Chronic Manganese Administration with Longer Intervals Between Injections Produced Neurotoxicity and Hepatotoxicity in Rats. *Neurochem Res*. Aug 2020;45(8):1941-1952. doi:10.1007/s11064-020-03059-2
20. Soto-Verdugo J, Ortega A. Critical Involvement of Glial Cells in Manganese Neurotoxicity. *Biomed Res Int*. 2021;2021:1596185. doi:10.1155/2021/1596185
21. Sidoryk-Wegrzynowicz M, Aschner M. Role of astrocytes in manganese mediated neurotoxicity. *BMC Pharmacol Toxicol*. Apr 18 2013;14:23. doi:10.1186/2050-6511-14-23
22. Kirkley KS, Popichak KA, Afzali MF, Legare ME, Tjalkens RB. Microglia amplify inflammatory activation of astrocytes in manganese neurotoxicity. *J Neuroinflammation*. May 5 2017;14(1):99. doi:10.1186/s12974-017-0871-0
23. Zhang P, Wong TA, Lokuta KM, Turner DE, Vujisic K, Liu B. Microglia enhance manganese chloride-induced dopaminergic neurodegeneration: role of free radical generation. *Exp Neurol*. May 2009;217(1):219-30. doi:10.1016/j.expneurol.2009.02.013

24. Popichak KA, Afzali MF, Kirkley KS, Tjalkens RB. Glial-neuronal signaling mechanisms underlying the neuroinflammatory effects of manganese. *J Neuroinflammation*. Nov 21 2018;15(1):324. doi:10.1186/s12974-018-1349-4
25. Frank-Cannon TC, Alto LT, McAlpine FE, Tansey MG. Does neuroinflammation fan the flame in neurodegenerative diseases? *Mol Neurodegener*. Nov 16 2009;4:47. doi:10.1186/1750-1326-4-47
26. Glass CK, Saijo K, Winner B, Marchetto MC, Gage FH. Mechanisms underlying inflammation in neurodegeneration. *Cell*. Mar 19 2010;140(6):918-34. doi:10.1016/j.cell.2010.02.016
27. Werner E, Gokhale A, Ackert M, et al. The mitochondrial RNA granule modulates manganese-dependent cell toxicity. *Mol Biol Cell*. Oct 1 2022;33(12):ar108. doi:10.1091/mbc.E22-03-0096
28. D'Souza AR, Minczuk M. Mitochondrial transcription and translation: overview. *Essays Biochem*. Jul 20 2018;62(3):309-320. doi:10.1042/EBC20170102
29. Murphy WI, Attardi B, Tu C, Attardi G. Evidence for complete symmetrical transcription in vivo of mitochondrial DNA in HeLa cells. *J Mol Biol*. Dec 25 1975;99(4):809-14. doi:10.1016/s0022-2836(75)80187-2
30. Santonoceto G, Jurkiewicz A, Szczesny RJ. RNA degradation in human mitochondria: the journey is not finished. *Hum Mol Genet*. May 22 2024;33(R1):R26-R33. doi:10.1093/hmg/ddae043
31. Barshad G, Marom S, Cohen T, Mishmar D. Mitochondrial DNA Transcription and Its Regulation: An Evolutionary Perspective. *Trends Genet*. Sep 2018;34(9):682-692. doi:10.1016/j.tig.2018.05.009
32. Chen YG, Hur S. Cellular origins of dsRNA, their recognition and consequences. *Nat Rev Mol Cell Biol*. Apr 2022;23(4):286-301. doi:10.1038/s41580-021-00430-1
33. Grochowska J, Czerwinska J, Borowski LS, Szczesny RJ. Mitochondrial RNA, a new trigger of the innate immune system. *Wiley Interdiscip Rev RNA*. May 2022;13(3):e1690. doi:10.1002/wrna.1690
34. Quadri M, Federico A, Zhao T, et al. Mutations in SLC30A10 cause parkinsonism and dystonia with hypermanganesemia, polycythemia, and chronic liver disease. *Am J Hum Genet*. Mar 9 2012;90(3):467-77. doi:10.1016/j.ajhg.2012.01.017
35. Tuschl K, Clayton PT, Gospe SM, Jr., et al. Syndrome of hepatic cirrhosis, dystonia, polycythemia, and hypermanganesemia caused by mutations in SLC30A10, a manganese transporter in man. *Am J Hum Genet*. Mar 9 2012;90(3):457-66. doi:10.1016/j.ajhg.2012.01.018
36. Zlatic SA, Werner E, Surapaneni V, et al. Systemic proteome phenotypes reveal defective metabolic flexibility in Mecp2 mutants. *Hum Mol Genet*. Dec 12 2023;33(1):12-32. doi:10.1093/hmg/ddad154
37. Lancaster MA, Corsini NS, Wolfinger S, et al. Guided self-organization and cortical plate formation in human brain organoids. *Nat Biotechnol*. Jul 2017;35(7):659-666. doi:10.1038/nbt.3906
38. Lane A, Gokhale A, Werner E, et al. Sulfur- and phosphorus-standardized metal quantification of biological specimens using inductively coupled plasma mass spectrometry. *STAR Protoc*. Jun 17 2022;3(2):101334. doi:10.1016/j.xpro.2022.101334
39. Zhang Y, Sloan SA, Clarke LE, et al. Purification and Characterization of Progenitor and Mature Human Astrocytes Reveals Transcriptional and Functional Differences with Mouse. *Neuron*. Jan 6 2016;89(1):37-53. doi:10.1016/j.neuron.2015.11.013
40. Marsh SE, Walker AJ, Kamath T, et al. Dissection of artifactual and confounding glial signatures by single-cell sequencing of mouse and human brain. *Nat Neurosci*. Mar 2022;25(3):306-316. doi:10.1038/s41593-022-01022-8

41. Xie Z, Bailey A, Kuleshov MV, et al. Gene Set Knowledge Discovery with Enrichr. *Curr Protoc*. Mar 2021;1(3):e90. doi:10.1002/cpz1.90
42. Wolf AR, Mootha VK. Functional genomic analysis of human mitochondrial RNA processing. *Cell Rep*. May 8 2014;7(3):918-31. doi:10.1016/j.celrep.2014.03.035
43. Schonborn J, Oberstrass J, Breyel E, Tittgen J, Schumacher J, Lukacs N. Monoclonal antibodies to double-stranded RNA as probes of RNA structure in crude nucleic acid extracts. *Nucleic Acids Res*. Jun 11 1991;19(11):2993-3000. doi:10.1093/nar/19.11.2993
44. Bonekamp NA, Peter B, Hillen HS, et al. Small-molecule inhibitors of human mitochondrial DNA transcription. *Nature*. Dec 2020;588(7839):712-716. doi:10.1038/s41586-020-03048-z
45. Chan CP, Jin DY. Cytoplasmic RNA sensors and their interplay with RNA-binding partners in innate antiviral response: theme and variations. *RNA*. Apr 2022;28(4):449-477. doi:10.1261/rna.079016.121
46. Dhir A, Dhir S, Borowski LS, et al. Mitochondrial double-stranded RNA triggers antiviral signalling in humans. *Nature*. Aug 2018;560(7717):238-242. doi:10.1038/s41586-018-0363-0
47. Arnaiz E, Miar A, Dias Junior AG, et al. Hypoxia Regulates Endogenous Double-Stranded RNA Production via Reduced Mitochondrial DNA Transcription. *Front Oncol*. 2021;11:779739. doi:10.3389/fonc.2021.779739
48. Luna-Sanchez M, Bianchi P, Quintana A. Mitochondria-Induced Immune Response as a Trigger for Neurodegeneration: A Pathogen from Within. *Int J Mol Sci*. Aug 7 2021;22(16)doi:10.3390/ijms22168523
49. Choi JP, Losol P, Ayoub G, et al. Cytokine Inductions and Intracellular Signal Profiles by Stimulation of dsRNA and SEB in the Macrophages and Epithelial Cells. *Immune Netw*. Apr 2022;22(2):e15. doi:10.4110/in.2022.22.e15
50. Shkundin A, Halaris A. IL-8 (CXCL8) Correlations with Psychoneuroimmunological Processes and Neuropsychiatric Conditions. *J Pers Med*. May 3 2024;14(5)doi:10.3390/jpm14050488
51. Erikson KM, Dobson AW, Dorman DC, Aschner M. Manganese exposure and induced oxidative stress in the rat brain. *Sci Total Environ*. Dec 1 2004;334-335:409-16. doi:10.1016/j.scitotenv.2004.04.044
52. Liberzon A, Birger C, Thorvaldsdottir H, Ghandi M, Mesirov JP, Tamayo P. The Molecular Signatures Database (MSigDB) hallmark gene set collection. *Cell Syst*. Dec 23 2015;1(6):417-425. doi:10.1016/j.cels.2015.12.004
53. Holzmann J, Frank P, Loffler E, Bennett KL, Gerner C, Rossmanith W. RNase P without RNA: identification and functional reconstitution of the human mitochondrial tRNA processing enzyme. *Cell*. Oct 31 2008;135(3):462-74. doi:10.1016/j.cell.2008.09.013
54. Szewczyk M, Malik D, Borowski LS, et al. Human REXO2 controls short mitochondrial RNAs generated by mtRNA processing and decay machinery to prevent accumulation of double-stranded RNA. *Nucleic Acids Res*. Jun 4 2020;48(10):5572-5590. doi:10.1093/nar/gkaa302
55. Wood LB, Winslow AR, Proctor EA, et al. Identification of neurotoxic cytokines by profiling Alzheimer's disease tissues and neuron culture viability screening. *Sci Rep*. Nov 13 2015;5:16622. doi:10.1038/srep16622
56. Geladi P, Kowalski BR. An example of 2-block predictive partial least-squares regression with simulated data. *Analytica Chimica Acta*. 1986/01/01/ 1986;185:19-32. doi:https://doi.org/10.1016/0003-2670(86)80029-0
57. Giovannoni F, Quintana FJ. The Role of Astrocytes in CNS Inflammation. *Trends Immunol*. Sep 2020;41(9):805-819. doi:10.1016/j.it.2020.07.007

58. Prajapati M, Zhang JZ, Chiu L, et al. Hepatic HIF2 is a key determinant of manganese excess and polycythemia in SLC30A10 deficiency. *JCI Insight*. Apr 23 2024;9(10)doi:10.1172/jci.insight.169738
59. Kim Y, Park J, Kim S, et al. PKR Senses Nuclear and Mitochondrial Signals by Interacting with Endogenous Double-Stranded RNAs. *Mol Cell*. Sep 20 2018;71(6):1051-1063 e6. doi:10.1016/j.molcel.2018.07.029
60. Sui H, Chen Q, Yang J, Srirattanapirom S, Imamichi T. Manganese enhances DNA- or RNA-mediated innate immune response by inducing phosphorylation of TANK-binding kinase 1. *iScience*. Nov 18 2022;25(11):105352. doi:10.1016/j.isci.2022.105352
61. Chan DW, Son SC, Block W, et al. Purification and characterization of ATM from human placenta. A manganese-dependent, wortmannin-sensitive serine/threonine protein kinase. *J Biol Chem*. Mar 17 2000;275(11):7803-10. doi:10.1074/jbc.275.11.7803
62. Bowman AB, Aschner M. Considerations on manganese (Mn) treatments for in vitro studies. *Neurotoxicology*. Mar 2014;41:141-2. doi:10.1016/j.neuro.2014.01.010
63. Taylor CA, Tuschl K, Nicolai MM, et al. Maintaining Translational Relevance in Animal Models of Manganese Neurotoxicity. *J Nutr*. Jun 1 2020;150(6):1360-1369. doi:10.1093/jn/nxaa066
64. Hasel P, Rose IVL, Sadick JS, Kim RD, Liddelow SA. Neuroinflammatory astrocyte subtypes in the mouse brain. *Nat Neurosci*. Oct 2021;24(10):1475-1487. doi:10.1038/s41593-021-00905-6
65. Endo F, Kasai A, Soto JS, et al. Molecular basis of astrocyte diversity and morphology across the CNS in health and disease. *Science*. Nov 4 2022;378(6619):eadc9020. doi:10.1126/science.adc9020
66. Chen Y, Colonna M. Microglia in Alzheimer's disease at single-cell level. Are there common patterns in humans and mice? *J Exp Med*. Sep 6 2021;218(9)doi:10.1084/jem.20202717
67. Paolicelli RC, Sierra A, Stevens B, et al. Microglia states and nomenclature: A field at its crossroads. *Neuron*. Nov 2 2022;110(21):3458-3483. doi:10.1016/j.neuron.2022.10.020
68. Sengupta A, Mense SM, Lan C, et al. Gene expression profiling of human primary astrocytes exposed to manganese chloride indicates selective effects on several functions of the cells. *Neurotoxicology*. May 2007;28(3):478-89. doi:10.1016/j.neuro.2006.10.005
69. Prajapati M, Quenneville CB, Zhang JZ, et al. AAV-mediated hepatic expression of SLC30A10 and the Thr95Ile variant attenuates manganese excess and other phenotypes in Slc30a10-deficient mice. *J Biol Chem*. Mar 2024;300(3):105732. doi:10.1016/j.jbc.2024.105732
70. Warden A, Mayfield RD, Gurol KC, Hutchens S, Liu C, Mukhopadhyay S. Loss of SLC30A10 manganese transporter alters expression of neurotransmission genes and activates hypoxia-inducible factor signaling in mice. *Metallomics*. Feb 7 2024;16(2)doi:10.1093/mtomcs/mfae007
71. Moreno JA, Yeomans EC, Streifel KM, Brattin BL, Taylor RJ, Tjalkens RB. Age-dependent susceptibility to manganese-induced neurological dysfunction. *Toxicol Sci*. Dec 2009;112(2):394-404. doi:10.1093/toxsci/kfp220
72. Viengkhou B, Hofer MJ. Breaking down the cellular responses to type I interferon neurotoxicity in the brain. *Front Immunol*. 2023;14:1110593. doi:10.3389/fimmu.2023.1110593
73. Dorrity TJ, Shin H, Gertie JA, Chung H. The Sixth Sense: Self-nucleic acid sensing in the brain. *Adv Immunol*. 2024;161:53-83. doi:10.1016/bs.ai.2024.03.001
74. Hosseini S, Michaelsen-Preusse K, Grigoryan G, Chhatbar C, Kalinke U, Korte M. Type I Interferon Receptor Signaling in Astrocytes Regulates Hippocampal Synaptic

Plasticity and Cognitive Function of the Healthy CNS. *Cell Rep*. May 19 2020;31(7):107666. doi:10.1016/j.celrep.2020.107666
75. Escoubas CC, Dorman LC, Nguyen PT, et al. Type-I-interferon-responsive microglia shape cortical development and behavior. *Cell*. Apr 11 2024;187(8):1936-1954 e24. doi:10.1016/j.cell.2024.02.020
76. Ejlerskov P, Hultberg JG, Wang J, et al. Lack of Neuronal IFN-beta-IFNAR Causes Lewy Body- and Parkinson's Disease-like Dementia. *Cell*. Oct 8 2015;163(2):324-39. doi:10.1016/j.cell.2015.08.069
77. Peixoto de Barcelos I, Jan AK, Modesti N, et al. Systemic complications of Aicardi Goutieres syndrome using real-world data. *Mol Genet Metab*. Sep-Oct 2024;143(1-2):108578. doi:10.1016/j.ymgme.2024.108578
78. Zhang P, Han B, Meng K, et al. Dystonia during pegylated interferon alpha therapy in a case with essential thrombocythemia and cerebral infarction. *Neurol Sci*. Dec 2024;45(12):5943-5945. doi:10.1007/s10072-024-07829-6
79. Paul BD, Snyder SH, Bohr VA. Signaling by cGAS-STING in Neurodegeneration, Neuroinflammation, and Aging. *Trends Neurosci*. Feb 2021;44(2):83-96. doi:10.1016/j.tins.2020.10.008
80. Lee H, Fenster RJ, Pineda SS, et al. Cell Type-Specific Transcriptomics Reveals that Mutant Huntingtin Leads to Mitochondrial RNA Release and Neuronal Innate Immune Activation. *Neuron*. Sep 9 2020;107(5):891-908 e8. doi:10.1016/j.neuron.2020.06.021
81. Lopez-Polo V, Maus M, Zacharioudakis E, et al. Release of mitochondrial dsRNA into the cytosol is a key driver of the inflammatory phenotype of senescent cells. *Nat Commun*. Aug 27 2024;15(1):7378. doi:10.1038/s41467-024-51363-0
82. Kim S, Tan S, Ku J, et al. RNA 5-methylcytosine marks mitochondrial double-stranded RNAs for degradation and cytosolic release. *Mol Cell*. Aug 8 2024;84(15):2935-2948 e7. doi:10.1016/j.molcel.2024.06.023
83. Peng T, Du SY, Son M, Diamond B. HIF-1alpha is a negative regulator of interferon regulatory factors: Implications for interferon production by hypoxic monocytes. *Proc Natl Acad Sci U S A*. Jun 29 2021;118(26)doi:10.1073/pnas.2106017118
84. Hooftman A, Peace CG, Ryan DG, et al. Macrophage fumarate hydratase restrains mtRNA-mediated interferon production. *Nature*. Mar 2023;615(7952):490-498. doi:10.1038/s41586-023-05720-6
85. O'Carroll SM, Peace CG, Toller-Kawahisa JE, et al. Itaconate drives mtRNA-mediated type I interferon production through inhibition of succinate dehydrogenase. *Nat Metab*. Nov 2024;6(11):2060-2069. doi:10.1038/s42255-024-01145-1

Figure legends

Figure 1: Manganese induces the accumulation of noncoding mitochondrial RNA sequences and mitochondrial dsRNA. **A)** Heatmaps of $\log_2$ CLTC normalized NanoString counts of RNA hybridized with probes targeted to non-coding sequences in the light strand transcripts and for nuclear encoded mitochondrial proteins as control. RNA was isolated from four replicate samples of either wild-type HAP1 or HeLa treated either in the absence or

presence of manganese (300µM and 800µM, respectively) for 24h, or untreated wild-type and SLC30A10 null HAP1 cells. Numbers in italics represent -log10 *p* values (t-test followed by Benjamini-Hochberg FDR correction, *q*). **B)** Manganese treatment and SLC30A10 deficiency similarly alter the MitoString transcriptome. Linear and non-linear data reduction by principal component analysis (PCA) and Uniform Manifold Approximation and Projection (UMAP), respectively of all the RNA counts measured by the MitoString panel. Lines connecting PCA represent Euclidean distances. **C)**Top Panel: Manganese was measured by ICP-MS at 24h post treatment in cell pellets of at least 3 independent experiments represented by different symbols, in brain cortex punch biopsies and liver of 8 weeks old wild type (WT) and *Slc30a10*$^{-/-}$ (KO) 3 female (◯) and 3 male (❑) mice. No sex differences were noted following two-way ANOVA test. Bottom Panel: Fold of change in metal content normalized by phosphate of HAP1 or HeLa cells treated in the absence or presence of manganese as in (a), were data from two experiments are combined and in wild type (WT) and *Slc30a10*$^{-/-}$ (KO) mouse cortex and liver. One-way ANOVA followed by Šídák's multiple comparisons test. **D)** Immunofluorescence detection of dsRNA and the mitochondrial RNA granule component, GSRF1, in HAP1 and HeLa cells treated either in the absence or presence of manganese. **E)** Quantification of dsRNA overlapping with GRSF1 in cells treated either in the absence or presence manganese, the POLMRT inhibitor IMT1 (1µM), or with dsRNA specific RNAse III before addition of the dsRNA J2 antibody. Dotted lines represent the average intensity of cells treated in the absence or presence manganese. One-way ANOVA followed by Šídák's multiple comparisons tests.

Figure 2: Manganese-induced dsRNA upregulates interferon β transcription. A) Diagram summarizing the pathway activated by manganese effects in mitochondria leading to IFNβ transcription. Depicted are the components targeted by inhibitors and the pathway agonists, poly (I:C) and ADU S100. Created with elements of Biorender.com. **B)** Interferon β promoter luciferase reporter activity measured in either HAP1 or HeLa cells following 24h treatment with the indicated manganese dose. For positive control 10µg/ml of high molecular weight poly (I:C) was added. Average ± SEM of 3 experiments. One-way ANOVA followed by Dunnett's multiple comparisons test. Dotted line marks luciferase activity in the absence of manganese. **C)** Interferon β promoter luciferase reporter activity measured in HeLa cells transfected with non-targeting and targeting siRNAs followed by 24h treatment with 800µM manganese or 10 µg/ml poly (I:C). Data are depicted as percentage of signal in scrambled sequence siRNA transfected cells. Average ± SEM of 3 experiments. Dotted line marks 50%

reduction. One-way ANOVA followed by Tukey's multiple comparisons test. Bottom panel depicts western blots of protein level downregulation following siRNA transfections. **D)** Top panel depicts manganese content determined by ICP-MS in HeLa cells incubated with 800µM manganese with and without the indicated inhibitor, identical conditions as employed for the bottom panel experiments. Bottom panel shows luciferase activity measured in HeLa cells following 24h treatment with the indicated manganese dose. For positive control, 10µg/ml of poly (I:C) were added. Average ± SEM of 5 experiments. Two-way ANOVA followed by Bonferroni's multiple comparisons test. **E)** Luciferase activity measured in HeLa cells following 24h treatment with 800µM manganese (top left panel) or 10µg/ml poly(I:C) (bottom left panel) in the presence or absence of the Sting inhibitor H-151. Right panel shows 0.5µM H-151 inhibition of luciferase induction by transfection of 1µM ADU S100 Sting agonist. Average± SE. Two-way ANOVA followed by Bonferroni's multiple comparisons test. Top numbers show manganese effect, bottom number show drug effect.

Figure 3: Manganese upregulates inflammatory cytokine secretion. A) Inflammatory cytokine antibody array probed with media conditioned for 48h collected from treated HeLa cells without or with 750µM manganese. **B)** Densitometry quantification of positive spots in the array blots shown in (a) and Supplementary Fig. 3A. **C)** IL-8 cytokine levels measured by ELISA in 48h conditioned media collected from HeLa cells treated without or with the indicated manganese concentration. Average ± SEM of 3 experiments. One-way ANOVA followed by Dunnett's multiple comparisons test. **D)** IL-8 cytokine levels measured by ELISA in 48h conditioned media collected from HeLa cells treated without or with 800µM manganese and the indicated inhibitor. Average ± SEM of 4 experiments. One-way ANOVA followed by Dunnett's multiple comparisons test. **E)** Cell survival of HeLa cells exposed to increased concentrations of manganese with and without the indicated inhibitor. Average ± SEM of 3-4 experiments. Two-way ANOVA followed by Bonferroni's multiple comparisons test.

Figure 4: Manganese alters mitochondrial transcripts and induces the interferon type I response in human cerebral organoids. A) Lineage marker expression measured by NanoString over developmental time. Average ± SEM of 4 organoids per time point. One-way ANOVA followed by Dunnett's multiple comparisons test. **B)** Heatmap of RNA levels of organoid differentiation markers and nuclear encoded mitochondrial transcripts measured by NanoString in individual organoids over time of development. Log_2 of normalized counts

of the gene were used for the heatmap. **C)** Heatmap of nuclear and mitochondrial encoded mitochondrial transcripts measured by NanoString in individual organoids over time of development. The difference of normalized counts from manganese-induced minus non-treated organoids per time point is expressed as Log_2. Non-responsive organelles at 30 days were compared to responses in 100-day organelles. Two-tailed t-test expressed as $-Log_{10}$. **D)** Volcano plot of the genes in the Neuroinflammatory panel that change expression in the transcriptome of 100-day organoids following 48h of 250µM manganese treatment. Significance threshold was set at 0.05 (marked by the line). **E)** Heatmap of IRF3 or NFκB transcriptional target genes and interferon stimulated genes included in the Neuroinflammatory panel (d) that change following manganese exposure. Two-tailed t-test expressed as $-Log_{10}$. **F)** Cytokines in conditioned media collected from 100-day organoids following mock or 48h treatment with 250µM manganese. IL6, IL8 and beta 2 microglobulin levels were determined by MesoScale assay. Average ± SEM. Each dot represents an individual organoid. Data from two organoid batches. Statistics for beta 2 microglobulin paired t test and for IL6 and IL8 Wilcoxon matched-pairs signed rank test. For B, C and E symbol size is proportional to the Log_2 value in between rows. Data available in Supplementary Information Dataset S1 and S2.

Figure 5: Single cell RNAseq analysis of manganese treated 100-day cerebral organoids. A) UMAP embedding of all samples (12 organoids aged 100 days) integrated and normalized with SCT transform. Cells are colored by cluster assignment. **B)** Proportion of cells assigned to each cluster from individual organoids. Color scheme is the same as in A). **C)** Dot plot of cell identity marker and inflammatory gene expression in cell clusters shown in A) (Supplementary Information Dataset S4). Dot size is proportional to percentage of cells expressing the gene and color reflects average expression level. **D)** Volcano plot of the manganese differentially regulated genes in astrocytes (Supplementary Information Dataset S5). Cut off is $p<0.05$ and $0.5<$ average log2FC <-0.5. Highlighted genes belong to the categories identified by gene enrichment analysis (e) or describing astrocyte function. **E)** Main up and down regulated pathways in manganese treated astrocytes when comparing the genes curated in Molecular Signatures Database employing EnrichR tool for gene ontology analysis (Supplementary Information Dataset S6). Triangles are up-regulated genes. Circles are downregulated genes. **F)** Heatmap of the scaled gene counts in the astrocyte cluster for individual organoids (Supplementary Information Dataset S7). **G)** Feature plot depicting the cells expressing CXCL8 and CXCL10 in control and manganese treated organoids. **H)**

UMAP embedding of the subclustered astrocyte population from all organoids. **J)** Differential expression of genes belonging to the interferon response, mitochondrial transcripts and RNA processing in the three astrocytes subclusters in response to manganese (Supplementary Information Dataset S8). **K)** Immunofluorescence for dsRNA in manganese treated 100-day organoids and in iPSC derived astrocytes. 1) 100-day organoids stained for GFAP (red), DNA (blue) and dsRNA (green). Scale bar= 25µm. 2) Quantification of the percentage of GFAP cells that were positive for dsRNA in (1) and dsRNA in mitochondria in iPSC derived astrocytes shown in (3).1.9x refers to fold of increase, Mann Whitney test 3) Human astrocytes derived from iPSC treated or not with 250µM Manganese for 24h and stained for dsRNA (green) and the mitochondrial marker TOM20 (red). Scale bar =10µm.

Fig 6: Cortex from a mouse model of hypermanganesemia with dystonia 1 disorder has increased pro-inflammatory cytokines. A) Heat map of *z*-scored cytokine levels measured by Luminex multiplex assays in cortex samples of wild type and *Slc30a10*$^{-/-}$ male and female mice. The cytokines are named by gene name. **B)** A discriminant partial least squares regression model constructed from the cytokine dataset regressed genotype. The model identifies a latent variable (LV1) that scores animals based on cytokine protein expression measurements and predicts genotype. LV2 describes variation that is not connected to genotype. LV1 and LV2 account for approximately 44% and 4% of the dataset variation, respectively. **C)** Top panel: LV1 is composed of cytokines that are elevated and able to predict the KO genotype in a leave-one-out cross validation in male mice samples (mean ± SD across LV1 generated for all models in the cross validation). Bottom panel: Comparison of LV1s from cortex and liver (in supplementary information) from *Slc30a10*$^{-/-}$ male animals. **D)** Volcano plots of TBP normalized NanoString counts of RNA isolated from brain of a cohort of 6 wild type and 6 *Slc30a10*$^{-/-}$ female and male mice, hybridized with probes targeted to neuroinflammatory gene sequences (Supplementary Information Dataset S9). **E)** Volcano plots of TBP normalized NanoString counts of RNA isolated from brain of a cohort of 3 wild type and 3 *Slc30a10*$^{-/-}$ male mice. **F)** Volcano plots of TBP normalized NanoString counts of RNA isolated from brain of a cohort of 3 wild type and 3 *Slc30a10*$^{-/-}$ female mice. Insert: Linear near data reduction by principal component analysis (PCA) of all the RNA counts measured by the neuroinflammatory panel separates the samples of both sexes by genotype. **G)** Heatmaps of interferon stimulated genes, genes expressed in astrocytes or in microglia, included in the Neuroinflammatory panel that change significantly

following manganese exposure (Supplementary Information Dataset 9). Two-tailed t-test expressed as $-Log_{10}$.

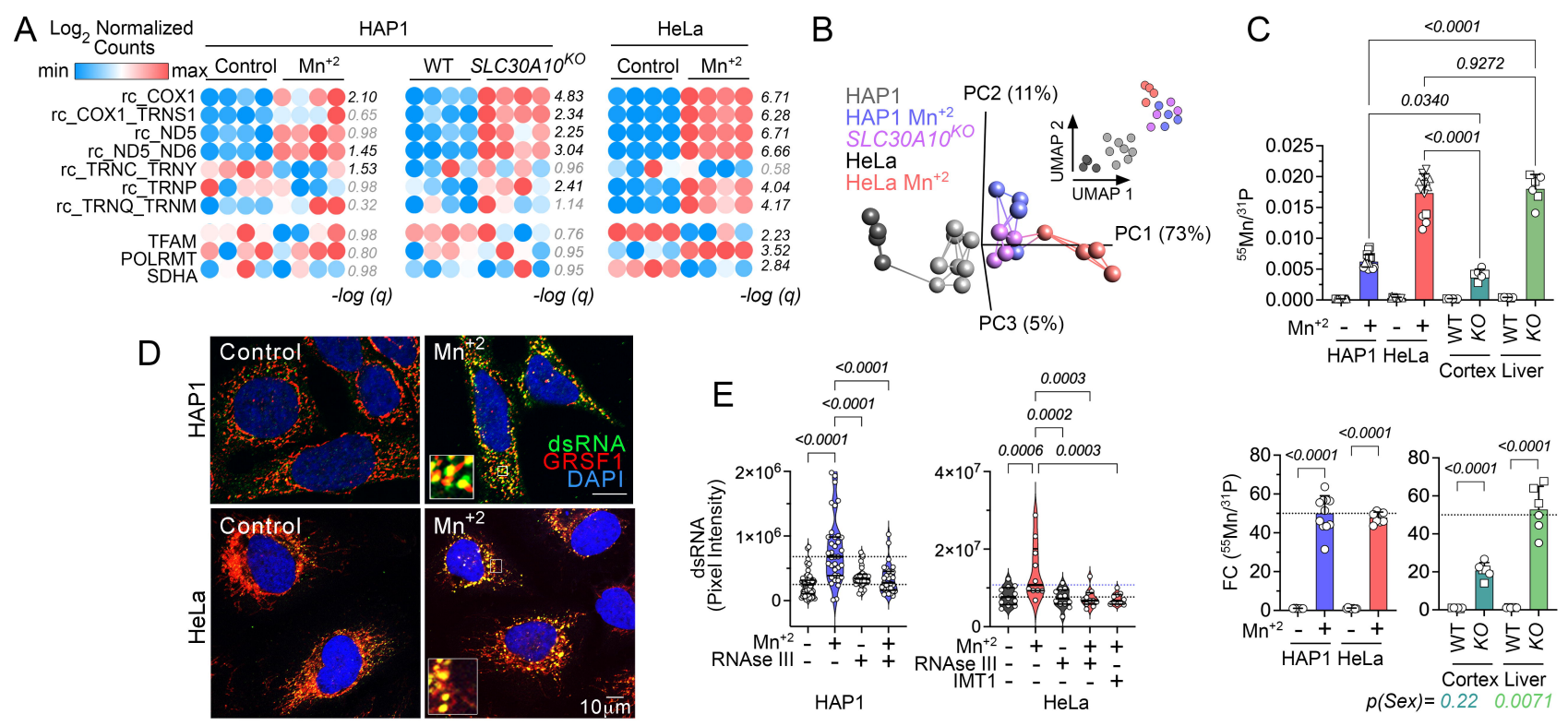
A
Log2 Normalized Counts
min
max
HAP1
HeLa
Control
Mn+2
WT
SLC30A10KO
rc_COX1
rc_COX1_TRNS1
rc_ND5
rc_ND5_ND6
rc_TRNC_TRNY
rc_TRNP
rc_TRNQ_TRNM
TFAM
POLRMT
SDHA
2.10
0.65
0.98
1.45
1.53
0.98
0.32
0.98
0.80
0.98
4.83
2.34
2.25
3.04
0.96
2.41
1.14
0.76
0.95
0.95
6.71
6.28
6.71
6.66
0.58
4.04
4.17
2.23
3.52
2.84
-log (q)
B
HAP1
HAP1 Mn+2
SLC30A10KO
HeLa
HeLa Mn+2
PC2 (11%)
PC1 (73%)
PC3 (5%)
UMAP 2
UMAP 1
C
<0.0001
0.9272
0.0340
<0.0001
55Mn/31P
Mn+2
HAP1
HeLa
WT
KO
Cortex
Liver
D
Control
Mn+2
HAP1
HeLa
dsRNA
GRSF1
DAPI
10µm
E
dsRNA (Pixel Intensity)
RNAse III
IMT1
HAP1
HeLa
FC (55Mn/31P)
p(Sex)= 0.22 0.0071

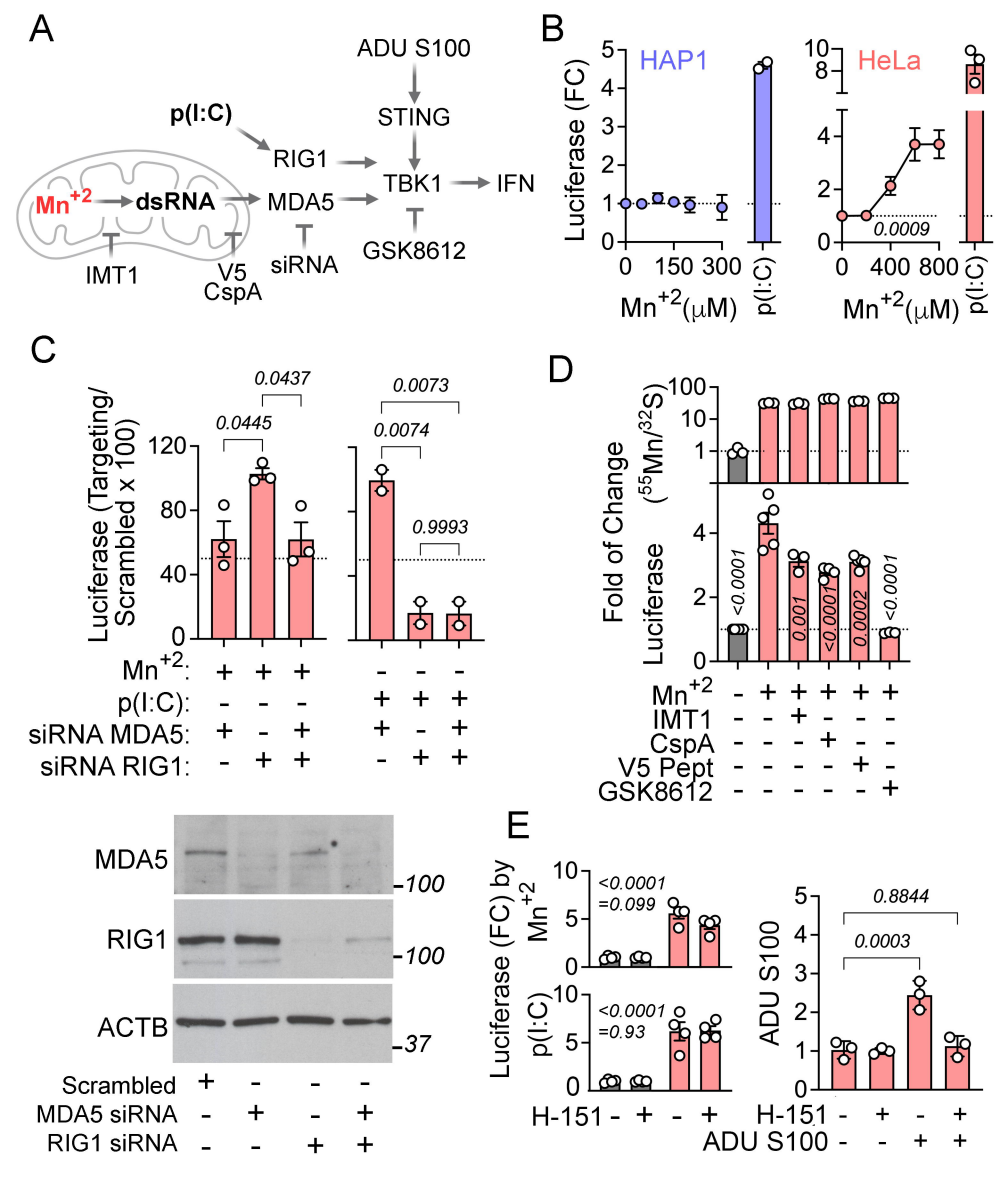
A
ADU S100
STING
p(I:C)
RIG1
TBK1
IFN
Mn+2
dsRNA
MDA5
IMT1
V5
CspA
siRNA
GSK8612
B
HAP1
HeLa
Luciferase (FC)
0.0009
Mn+2(μM)
p(I:C)
C
Luciferase (Targeting/ Scrambled x 100)
0.0445
0.0437
0.0074
0.0073
0.9993
Mn+2:
p(I:C):
siRNA MDA5:
siRNA RIG1:
D
Fold of Change (55Mn/32S)
Luciferase
<0.0001
0.001
<0.0001
0.0002
<0.0001
Mn+2
IMT1
CspA
V5 Pept
GSK8612
MDA5
RIG1
ACTB
100
100
37
Scrambled
MDA5 siRNA
RIG1 siRNA
E
Luciferase (FC) by Mn+2
<0.0001
=0.099
p(I:C)
<0.0001
=0.93
ADU S100
0.8844
0.0003
H-151
ADU S100

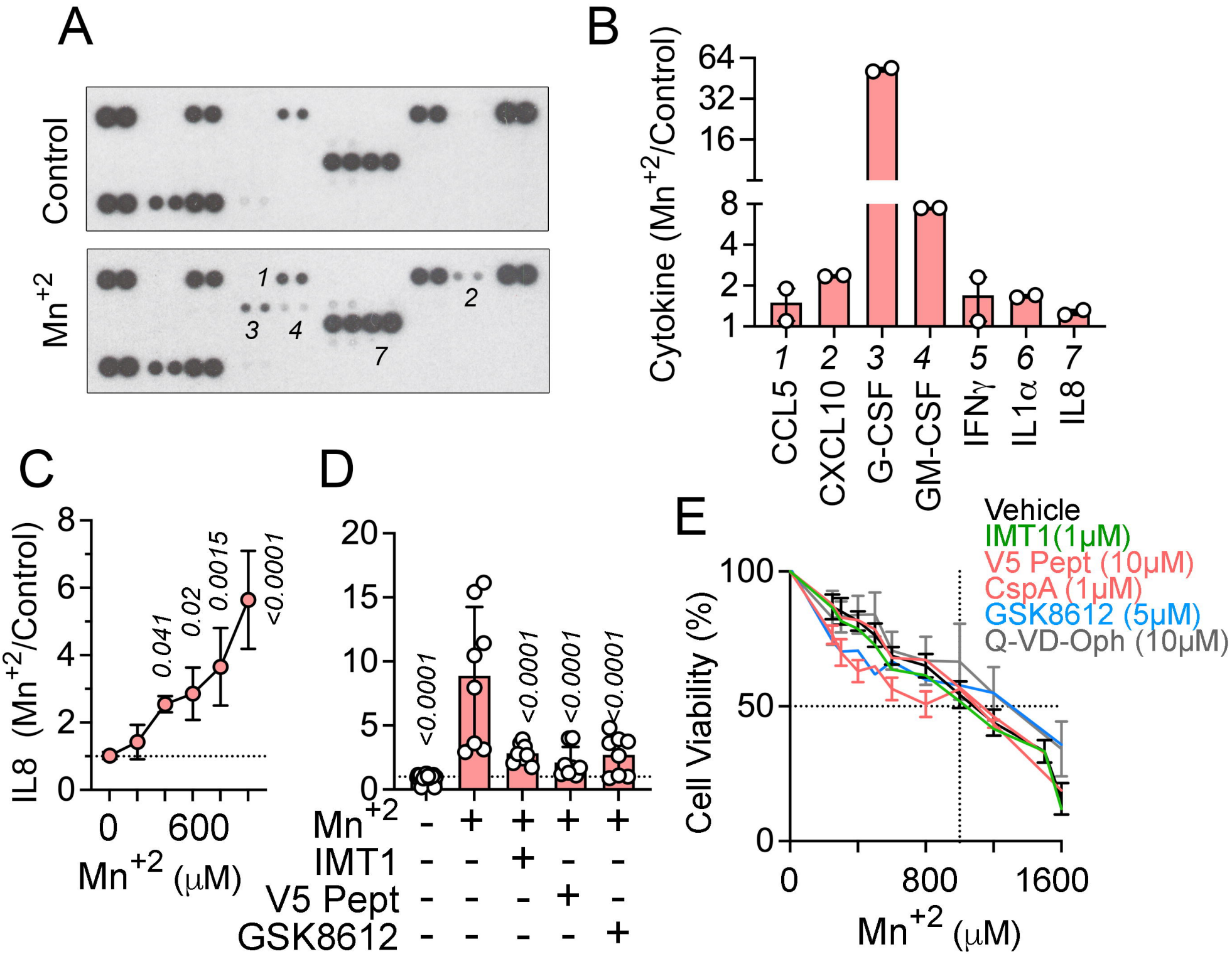
A
Control
Mn+2
1
2
3
4
7
B
Cytokine (Mn+2/Control)
64
32
16
8
4
2
1
1 CCL5
2 CXCL10
3 G-CSF
4 GM-CSF
5 IFNγ
6 IL1α
7 IL8
C
IL8 (Mn+2/Control)
8
6
4
2
0
0.041
0.02
0.0015
<0.0001
0
600
Mn+2 (μM)
D
20
15
10
5
0
<0.0001
<0.0001
<0.0001
<0.0001
Mn+2 - + + + +
IMT1 - - + - -
V5 Pept - - - + -
GSK8612 - - - - +
E
Vehicle
IMT1(1μM)
V5 Pept (10μM)
CspA (1μM)
GSK8612 (5μM)
Q-VD-Oph (10μM)
Cell Viability (%)
100
50
0
0
800
1600
Mn+2 (μM)

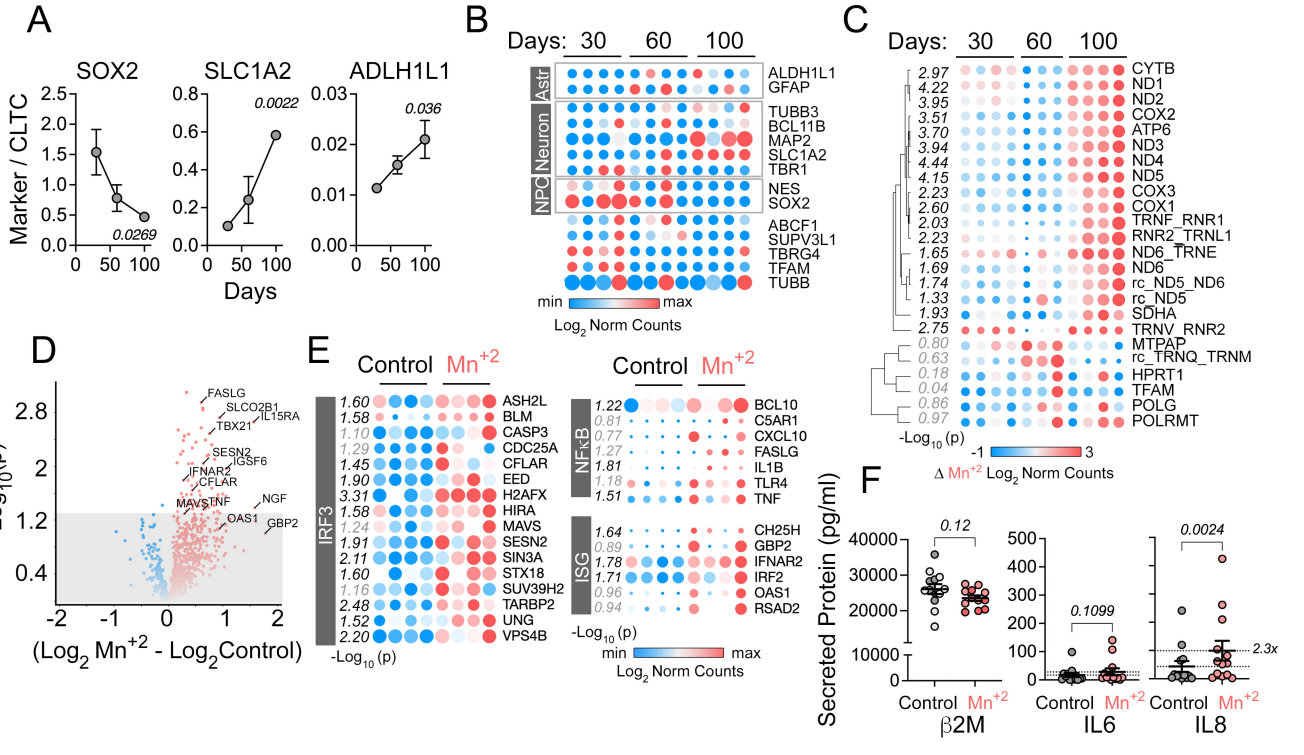
A
SOX2
SLC1A2
ADLH1L1
Marker / CLTC
0.0269
0.0022
0.036
Days
B
Days: 30 60 100
Astr
Neuron
NPC
ALDH1L1
GFAP
TUBB3
BCL11B
MAP2
SLC1A2
TBR1
NES
SOX2
ABCF1
SUPV3L1
TBRG4
TFAM
TUBB
min
max
Log2 Norm Counts
C
Days: 30 60 100
CYTB
ND1
ND2
COX2
ATP6
ND3
ND4
ND5
COX3
COX1
TRNF_RNR1
RNR2_TRNL1
ND6_TRNE
ND6
rc_ND5_ND6
rc_ND5
SDHA
TRNV_RNR2
MTPAP
rc_TRNQ_TRNM
HPRT1
TFAM
POLG
POLRMT
-Log10 (p)
Δ Mn+2 Log2 Norm Counts
D
FASLG
SLCO2B1
IL15RA
TBX21
SESN2
IGSF6
IFNAR2
CFLAR
MAVS
TNF
NGF
OAS1
GBP2
-Log10(p)
(Log2 Mn+2 - Log2Control)
E
Control
Mn+2
IRF3
ASH2L
BLM
CASP3
CDC25A
CFLAR
EED
H2AFX
HIRA
MAVS
SESN2
SIN3A
STX18
SUV39H2
TARBP2
UNG
VPS4B
-Log10 (p)
NFκB
BCL10
C5AR1
CXCL10
FASLG
IL1B
TLR4
TNF
ISG
CH25H
GBP2
IFNAR2
IRF2
OAS1
RSAD2
min
max
Log2 Norm Counts
F
Secreted Protein (pg/ml)
0.12
0.1099
0.0024
2.3x
Control
Mn+2
β2M
IL6
IL8

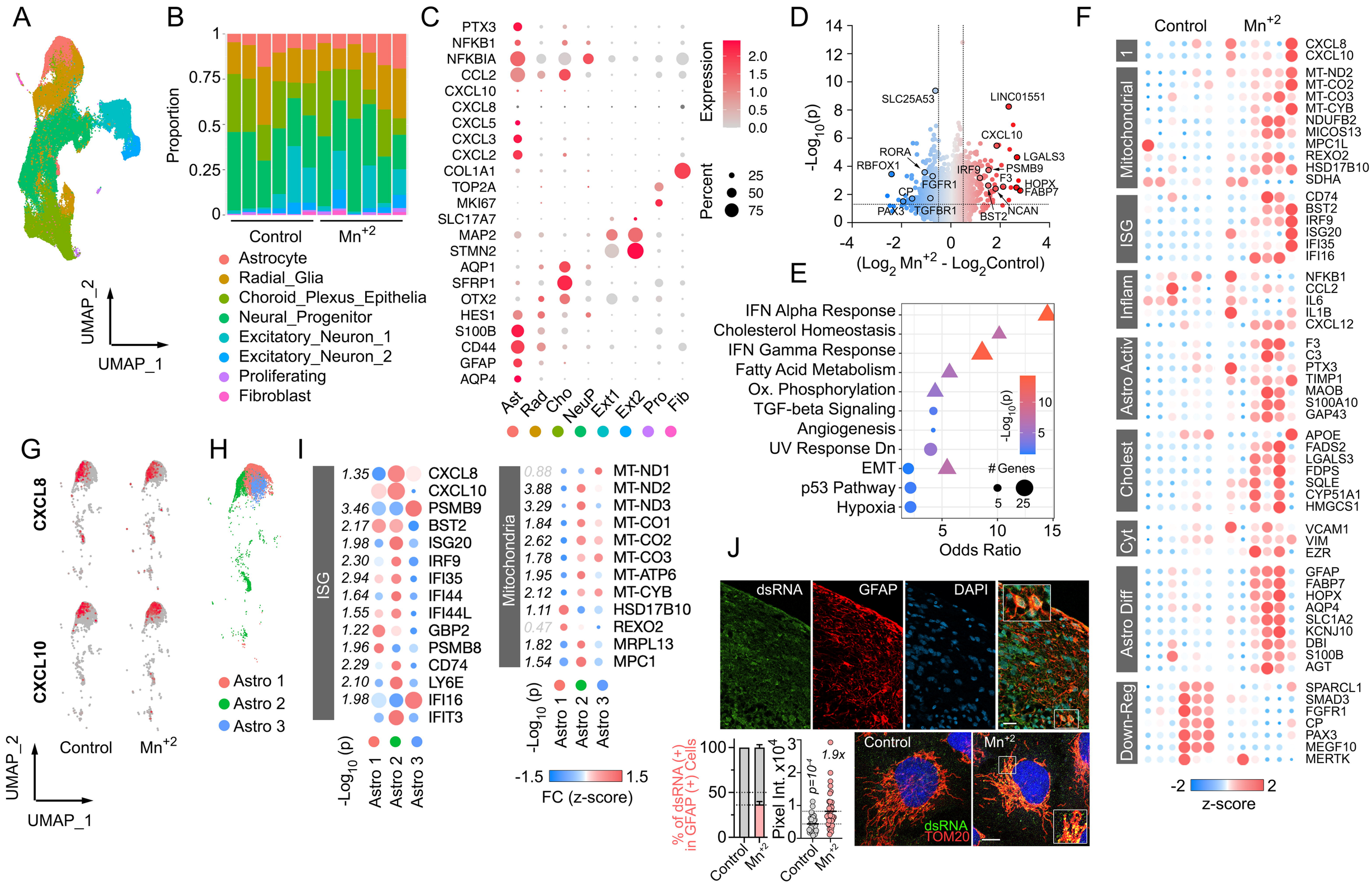
A
UMAP_2
UMAP_1
B
Proportion
Control
Mn+2
Astrocyte
Radial_Glia
Choroid_Plexus_Epithelia
Neural_Progenitor
Excitatory_Neuron_1
Excitatory_Neuron_2
Proliferating
Fibroblast
C
PTX3
NFKB1
NFKBIA
CCL2
CXCL10
CXCL8
CXCL5
CXCL3
CXCL2
COL1A1
TOP2A
MKI67
SLC17A7
MAP2
STMN2
AQP1
SFRP1
OTX2
HES1
S100B
CD44
GFAP
AQP4
Ast
Rad
Cho
NeuP
Ext1
Ext2
Pro
Fib
Expression
Percent
D
-Log10(p)
(Log2 Mn+2 - Log2Control)
SLC25A53
LINC01551
CXCL10
LGALS3
RORA
RBFOX1
IRF9
PSMB9
F3
HOPX
FABP7
FGFR1
CP
PAX3
TGFBR1
BST2
NCAN
E
IFN Alpha Response
Cholesterol Homeostasis
IFN Gamma Response
Fatty Acid Metabolism
Ox. Phosphorylation
TGF-beta Signaling
Angiogenesis
UV Response Dn
EMT
p53 Pathway
Hypoxia
-Log10(p)
Genes
Odds Ratio
F
Control
Mn+2
1
Mitochondrial
ISG
Inflam
Astro Activ
Cholest
Cyt
Astro Diff
Down-Reg
CXCL8
CXCL10
MT-ND2
MT-CO2
MT-CO3
MT-CYB
NDUFB2
MICOS13
MPC1L
REXO2
HSD17B10
SDHA
CD74
BST2
IRF9
ISG20
IFI35
IFI16
NFKB1
CCL2
IL6
IL1B
CXCL12
F3
C3
PTX3
TIMP1
MAOB
S100A10
GAP43
APOE
FADS2
LGALS3
FDPS
SQLE
CYP51A1
HMGCS1
VCAM1
VIM
EZR
GFAP
FABP7
HOPX
AQP4
SLC1A2
KCNJ10
DBI
S100B
AGT
SPARCL1
SMAD3
FGFR1
CP
PAX3
MEGF10
MERTK
z-score
G
CXCL8
CXCL10
Control
Mn+2
UMAP_2
UMAP_1
H
Astro 1
Astro 2
Astro 3
I
ISG
1.35 CXCL8
CXCL10
3.46 PSMB9
2.17 BST2
1.98 ISG20
2.30 IRF9
2.94 IFI35
1.64 IFI44
1.55 IFI44L
1.22 GBP2
1.96 PSMB8
2.29 CD74
2.10 LY6E
1.98 IFI16
IFIT3
Mitochondria
0.88 MT-ND1
3.88 MT-ND2
3.29 MT-ND3
1.84 MT-CO1
2.62 MT-CO2
1.78 MT-CO3
1.95 MT-ATP6
2.12 MT-CYB
1.11 HSD17B10
0.47 REXO2
1.82 MRPL13
1.54 MPC1
-Log10 (p)
Astro 1
Astro 2
Astro 3
-1.5
1.5
FC (z-score)
J
dsRNA
GFAP
DAPI
% of dsRNA (+) in GFAP (+) Cells
Pixel Int. x10^4
p=10^-4
1.9x
Control
Mn+2
dsRNA
TOM20

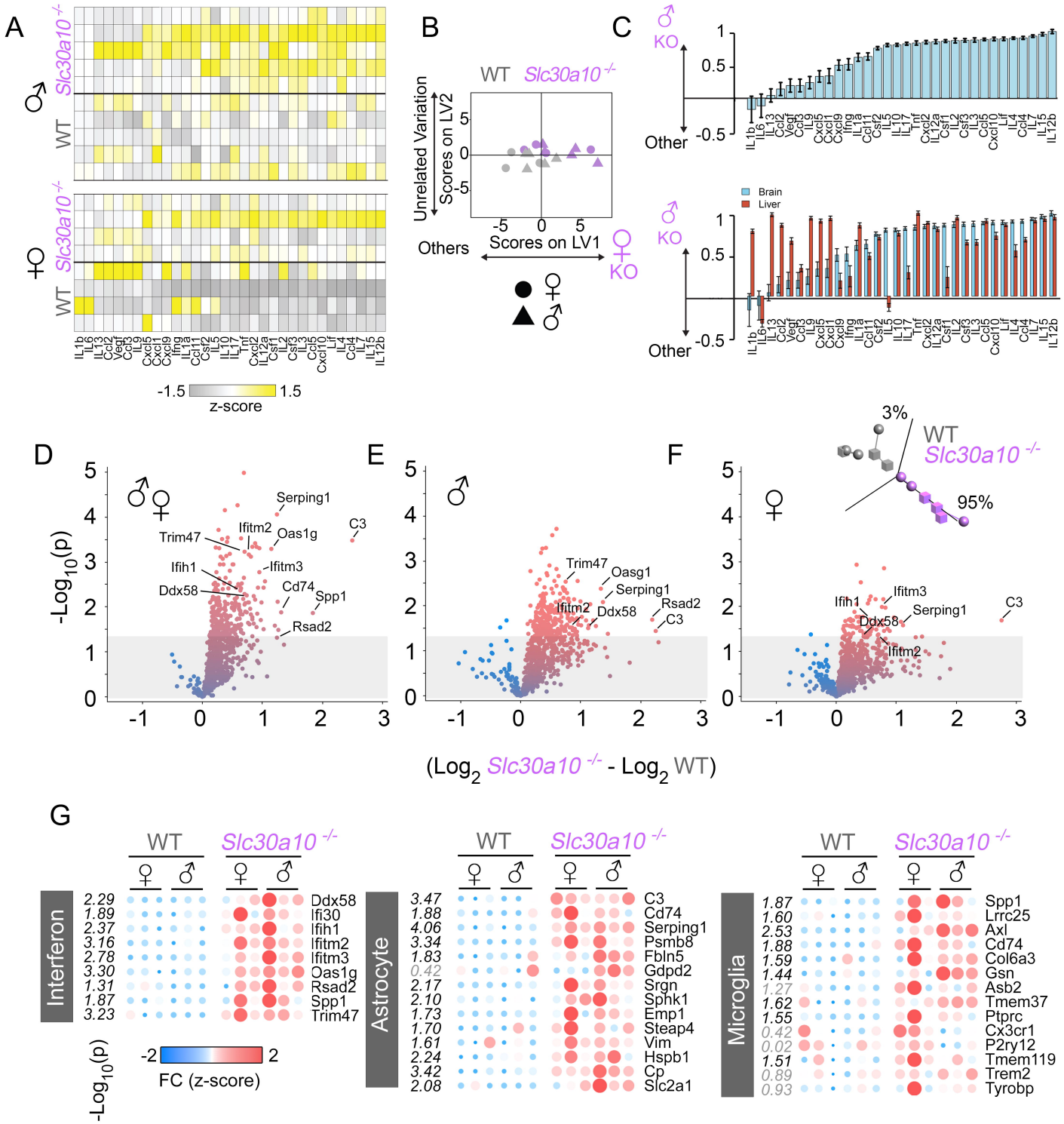
A
Slc30a10 -/-
♂
WT
Slc30a10 -/-
♀
WT
IL1b IL6 IL13 Ccl2 Vegf Ccl3 Il9 Cxcl5 Cxcl1 Cxcl9 Ifng IL1a Ccl11 Csf2 IL5 IL10 IL17 Tnf Cxcl2 IL12a Csf1 IL2 Csf3 IL3 Ccl5 Cxcl10 Lif IL4 Ccl4 IL7 IL15 IL12b
-1.5
1.5
z-score
B
WT
Slc30a10 -/-
Unrelated Variation
Scores on LV2
Scores on LV1
Others
♀ KO
♀
♂
C
♂ KO
Other
Brain
Liver
D
E
F
Serping1
Ifitm2
Oas1g
C3
Trim47
Ifitm3
Ifih1
Cd74
Ddx58
Spp1
Rsad2
Oasg1
3%
95%
WT
Slc30a10 -/-
-Log10(p)
(Log2 Slc30a10 -/- - Log2 WT)
G
WT
Slc30a10 -/-
Interferon
2.29 Ddx58
1.89 Ifi30
2.37 Ifih1
3.16 Ifitm2
2.78 Ifitm3
3.30 Oas1g
1.31 Rsad2
1.87 Spp1
3.23 Trim47
Astrocyte
3.47 C3
1.88 Cd74
4.06 Serping1
3.34 Psmb8
1.83 Fbln5
0.42 Gdpd2
2.17 Srgn
2.10 Sphk1
1.73 Emp1
1.70 Steap4
1.61 Vim
2.24 Hspb1
3.42 Cp
2.08 Slc2a1
Microglia
1.87 Spp1
1.60 Lrrc25
2.53 Axl
1.88 Cd74
1.59 Col6a3
1.44 Gsn
1.27 Asb2
1.62 Tmem37
1.55 Ptprc
0.42 Cx3cr1
0.02 P2ry12
1.51 Tmem119
0.89 Trem2
0.93 Tyrobp
-2
2
FC (z-score)
-Log10(p)